Insight into contraction dynamics of microwave plasmas for CO_2 conversion from plasma chemistry modelling

P. Viegas[1], L. Vialetto[1], A. J. Wolf[1], F. J. J. Peeters[1], P. W. C. Groen[1], T. W. H. Righart[1], W. A. Bongers[1], M. C. M van de Sanden[1,2] and P. Diomede[1]

[1] DIFFER - Dutch Institute for Fundamental Energy Research, 5612 AJ Eindhoven, The Netherlands
[2] Department of Applied Physics, Eindhoven University of Technology, P. O. Box 513, 5600 MB Eindhoven, The Netherlands

E-mail: `p.viegas@differ.nl`

28 July 2020

Abstract. This work addresses plasma chemistry in the core of a vortex-stabilized microwave discharge for CO_2 conversion numerically, focusing on the pressure-dependent contraction dynamics of this plasma. A zero-dimensional model is presented for experimental conditions in a pressure range between 60 and 300 mbar and a temperature range between 3000 and 6500 K. Monte Carlo Flux simulations, which describe electron kinetics, are self-consistently coupled to the plasma chemistry model. The simulation results show that an increase in pressure is accompanied by a transition in neutral composition in the plasma core: from a significant amount of CO_2 and O_2 at low pressures to a O/CO/C mixture at high pressures, the composition being determined mostly by thermal equilibrium and by transport processes. The change of temperature and composition with pressure lead to higher ionisation coefficient and more atomic ion composition in the plasma core. These changes result in an increase in ionisation degree in the plasma core from 10^{-5} to 10^{-4}. These factors are shown to be fundamental to drive contraction in the CO_2 microwave discharge.

Keywords: CO_2 plasma chemistry, microwave discharge, discharge contraction, CO_2 conversion

1. Introduction

In recent years, much attention has been dedicated to low-temperature plasmas to convert greenhouse gas CO_2 into carbon-neutral fuels or useful chemicals [*Goede et al.*, 2014; *Goede and van de Sanden*, 2016; *Guerra et al.*, 2017; *Snoeckx and Bogaerts*, 2017]. In this context, experimental studies of microwave (MW) discharges have provided the most promising results. In the 1970s and 1980s, high energy efficiencies of up to 80% have been reported by experimental investigations in subsonic vortex-confined MW reactors under proposed conditions of strong vibrational-translational nonequilibrium [*Legasov et al.*, 1978; *Butylkin et al.*, 1981; *Asisov et al.*, 1981; *Fridman and Kennedy*, 2004; *Fridman*, 2008]. More recently, experimental investigations in similar conditions have reported high gas temperatures in the plasma core above 3000 K, energy efficiencies up to 50% and conversion efficiencies up to 80% [*van Rooij et al.*, 2015; *den Harder et al.*, 2017; *Bongers et al.*, 2017; *van den Bekerom et al.*, 2019]. The optimal conditions for these MW plasma reactors have shown a strong correlation with pressure and discharge contraction dynamics. Indeed, record efficiencies have been registered at pressures between 100 and 200 mbar, coinciding with transitions from radially diffuse to contracted discharge structures [*Fridman*, 2008; *van Rooij et al.*, 2015; *den Harder et al.*, 2017]. Despite the important implications of discharge contraction phenomena, the discharge contraction mechanisms in molecular plasmas of changing composition remain largely unexplored.

Plasma contraction has been widely observed in both DC and AC discharges at moderate to high pressures and studied through experiments and models, especially with noble gases. Among the most generally accepted mechanisms to explain the phenomenon of contraction in conditions of subatmospheric pressure there is the influence of finite thermal conductivity on molecular ions. As pressure increases, charge-balance in electropositive discharges becomes dominated by electron-ion recombination. Furthermore, temperature increases in the centre and sharper temperature gradients are formed between the walls and the centre than at lower pressures, ensuring more dissociation of molecular ions in the centre than near the walls. Then, the loss of electrons by volume dissociative recombination is higher in the outer regions and electron density is higher in the centre, resulting in a contracted plasma. This mechanism has been reported, at least, in DC glow discharges with Xe, Kr, Ar and mixtures of these gases with small quantities of N_2 [*Kenty*, 1962], and in surface-wave microwave discharges with Ar [*Martinez et al.*, 2004; *Ridenti et al.*, 2018], Kr and Ne [*Kabouzi et al.*, 2002; *Moisan and Pelletier*, 2012]. *Martinez et al.* [2009] have confirmed this mechanism by reporting experimental evidence that when a small amount ($< 1\%$) of a noble gas having a lower ionisation potential (Kr or Ar) is added to a contracted Ne discharge, the contracted discharge expands radially, due to the predominance of atomic ions of the added gas. However, other factors can limit or enhance contraction. *Kabouzi et al.* [2002] and *Wolf et al.* [2019] have proposed, based on measurements in microwave discharges, that the plasma radius is limited by the skin-depth of wave absorption. Power absorption

is thus concentrated in a smaller volume in a contracted discharge than in a more diffuse one. Moreover, the non-uniform gas heating in contracted plasmas is enhanced by the positive feedback between heating and increasing electron density and reduced electric field, also called thermal-ionisation instability [*Shneider et al.*, 2012, 2014; *Zhong et al.*, 2019]. In the numerical works by *Shneider et al.* [2012, 2014] with N_2 and air DC glow discharges, this effect is sufficient to describe contraction, even whithout considering atomic ions. A self-reinforcing cycle between ionisation and the role of increasing electron-electron collisions on the EEDF is also claimed to contribute to contraction in DC glow discharges with Ar and Ne [*Petrov and Ferreira*, 1999; *Dyatko et al.*, 2008; *Golubovskii et al.*, 2011]. In the recent experimental work by *Golubovskii et al.* [2019], this cycle has been shown to lead to contraction in these gases even without non-uniform heating. On the other hand, in *Golubovskii et al.* [2020] the contraction dynamics in He discharges has been attributed to non-uniform gas heating without influence of charged particle kinetics. Despite the extensive literature, the implications of chemical reactions on plasma contraction dynamics in reactive mixtures of changing composition have been studied only recently. In *Zhong et al.* [2019], the implications of chemical reactions on discharge contraction have been described in a numerical study on reactive $H_2/O_2/N_2$ mixtures in a DC glow discharge. It has been found that the thermo-chemical heat exchange, which is a result of endothermic and exothermic reactions, induces stability and instability, respectively, of the discharge modes. *Zhong et al.* [2019] have shown that the mixture composition can have a large influence on discharge contraction, through its relationship with heat exchange and its influence on charged particle kinetics, both impacting the thermal-ionisation instability.

Concerning vortex-stabilized CO_2 MW plasma, its contraction has been investigated in *Wolf et al.* [2019] in the pressure range up to 400 mbar in relation to its dielectric properties. It has been found that the discharge column has a radius of approximately a single skin-depth of wave absorption. By measuring the electron density (n_e) and gas temperature, this work has shown that the discharge radius (r_d) and the ionisation degree of the plasma core (n_e over gas density N_g) are interdependent, following the relationship: $n_e/N_g \propto r_d^{-2}$. Then, in *Wolf et al.* [2020], in the same CO_2 plasma, three distinct discharge modes have been identified and described. A homogeneous mode has been identified below 85 mbar, due to the suppression of contraction by an absorption cut-off of the microwave field at the critical electron density that imposes microwave reflection and under-dense conditions. For collisional conditions at higher pressures, two contracted discharge modes have been described: low confinement L-mode at temperatures between 3000 and 4000 K and high confinement H-mode at temperatures between 5500 and 6500 K, which respectively correspond to the thermal dissociation thresholds of CO_2 and CO. A hybrid regime occurs in the transition between L- and H-modes. The stability of the contracted modes has been found to arise under conditions of high reactive heat capacity, while the instability in the transition in between modes takes place under conditions of low heat capacity. As such, the favourable conditions for efficient plasma-driven conversion of CO_2 in hybrid

regime have been explained in *Wolf et al.* [2020] by the increasing CO production in the plasma core with rising pressure in L-mode and increasing CO recombination pathways with pressure in H-mode. Moreover, it has been proposed that the modes are determined by the thermally driven chemical conversion of the plasma, following generally the same contraction mechanisms as in *Zhong et al.* [2019]. The difference in the spatial structure of the L- and H- contracted modes is claimed to result from the evolution of charged particle kinetics in response to the shifting chemical composition. In *Groen et al.* [2019], three-dimensional electromagnetic modelling has been used to assess this system. However, the dominant charged particle kinetics in relation to the contraction dynamics in CO_2 at high temperatures remains largely unexplored.

The elevated temperatures associated with the contraction of the CO_2 MW discharge (3000 to 6500 K) lead to a wide variety of species in the plasma. Several modelling studies have addressed CO_2 plasma chemistry in conditions of high temperature and high dissociation degree [*Butylkin et al.*, 1979; *Park et al.*, 1994; *Beuthe and Chang*, 1997; *Berthelot and Bogaerts*, 2016; *Wang and Bogaerts*, 2016; *Wang et al.*, 2016; *Trenchev et al.*, 2017; *Sun et al.*, 2017; *Kotov and Koelman*, 2019; *Pietanza et al.*, 2020]. However, these are usually limited by the neglection of one or several of the following factors: atomic ions, ion transfers or validation against experimental measurements of discharge parameters. A recent work of plasma chemistry modelling [*Pietanza et al.*, 2020] has simulated the plasma described in *Groen et al.* [2019], finding a qualitative agreement with the measured electron density and estimated E/N_g and T_e. Nevertheless, the results in *Pietanza et al.* [2020] suggest that the neutral composition in the CO_2 MW plasma is not essentially determined by thermal equilibrium, which contradicts the assumptions so far [*den Harder et al.*, 2017; *van den Bekerom et al.*, 2019; *Groen et al.*, 2019; *Wolf et al.*, 2019, 2020]. As a result, a state-of-the-art reaction scheme for the conditions of interest in CO_2 MW discharges is lacking, as well as an understanding of the dominant charged particle processes in these plasmas.

The importance of controlling the discharge modes in optimizing the plasma processing conditions motivates further investigation into the contraction dynamics. This paper addresses the charged particle kinetics associated with the contraction dynamics in the moderate-to-high pressure CO_2 microwave discharge. Section 2 presents a set of measurements related to the contraction dynamics in the same experimental conditions as in *Wolf et al.* [2019]. Then, in section 3, a zero-dimensional plasma chemistry model is presented, representing the plasma core and addressing relevant neutral and charged particle kinetics in conditions of experiments, as well as an estimation of transport processes. Moreover, the coupling between the plasma chemistry model and the Monte Carlo Flux method for electron kinetics is described. The results of this model are compared in section 4 with the experimentally estimated peak power density. Then, the model is used to obtain insight on neutral composition and ion composition in the plasma core and on the mechanisms determining the changes in ionisation degree associated to the contraction dynamics. Finally, the effect of the uncertainty of input parameters on the numerical results is assessed.

2. Experimental set-up

The experimental discharges are obtained in a vortex-stabilized microwave reactor, a configuration commonly used for plasma-driven CO_2 conversion [*Butylkin et al.*, 1981; *Fridman*, 2008; *Bongers et al.*, 2017]. The setup is described in *Wolf et al.* [2019] and consists of a 2.45 GHz microwave source, a rectangular waveguide field applicator and a 3-stub tuner for impedance matching. The electromagnetic (EM) field is coupled to a CO_2 gas flow, which is contained in a quartz tube of 27 mm inner diameter that intersects the waveguide through the center of its broad side (in the direction parallel to the TE_{10} single mode standing wave). The wave electric field is thus directed parallel to the discharge tube. The plasma is stabilized in the center of the tube by means of a vortex flow, obtained through tangential gas injection, to prevent plasma-induced wall damage, as in *Fleisch et al.* [2007]. Besides the stabilizing effect resulting from radial heat transfer, this kind of flow has been shown to increase efficiency in a microwave reactor for the abatement of perfluorinated compound (PFC) gases [*Nantel-Valiquette et al.*, 2006]. This is claimed to be due to the optimisation of the volume of interaction between contracted plasma and PFC gases.

The experimental conditions considered in this work are based on previously reported measurements [*Wolf et al.*, 2019], obtained at a fixed steady-state input power of 1.4 kW and a flow rate of 18 slm. The pressure range between 60 and 296 mbar is considered in order to cover three distinct discharge modes, i.e. the homogeneous, L-mode and H-mode regimes, represented in figure 1, each of which is characterised by distinct plasma parameters. A hybrid regime also occurs, which exhibits H-mode conditions in the central region of the filament while simultaneously exhibiting L-mode conditions axially outwards.
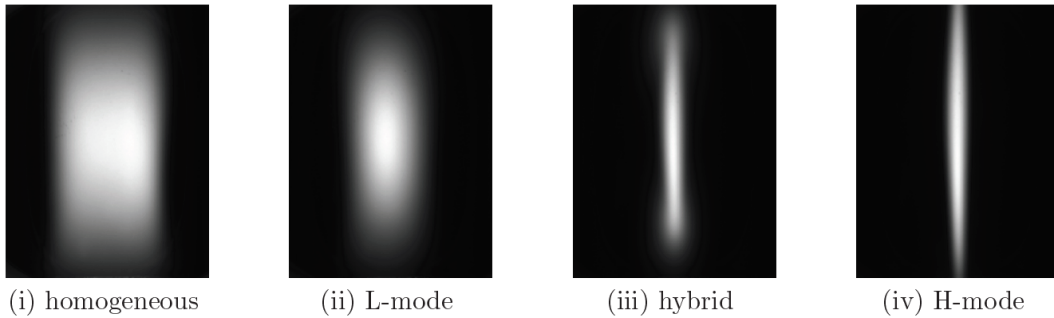

(i) homogeneous   (ii) L-mode   (iii) hybrid   (iv) H-mode

Figure 1. Visual appearance of the CO_2 microwave discharge in several distinct modes, which shows an increasing radial contraction of the discharge (from left to right) with rising pressure. Images adapted from *Wolf et al.* [2020].

An overview of relevant discharge parameters is shown in tables 1 and 2 for 9 pressure (p) conditions. The peak values of electron density (n_e) and gas temperature (T_g) in the center of the plasma are based, respectively, on 168 GHz microwave interferometry and Doppler broadening of the spectral peak of the $O(3s^5S^0 \leftarrow 3p^5P)$ 777 nm triplet lines of atomic oxygen [*Wolf et al.*, 2019]. The measured radial profiles

p [mbar]	$T_g \pm \delta_{T_g}$ [K]	$n_e \pm \delta_{n_e}$ [cm^{-3}]	P_{abs} [W cm^{-3}]	Regime
60	3322 ± 121	$(0.8 \pm 1.1) \times 10^{12}$	312	Homogeneous
97	4677 ± 196	$(1.1 \pm 1.6) \times 10^{12}$	1109	L-mode
108	5384 ± 247	$(2.7 \pm 3.1) \times 10^{12}$	3043	Hybrid
121	5852 ± 225	$(9.0 \pm 4.4) \times 10^{12}$	3430	Hybrid
141	6207 ± 216	$(2.0 \pm 0.5) \times 10^{13}$	4370	Hybrid
161	6225 ± 233	$(1.8 \pm 0.5) \times 10^{13}$	4725	H-mode
209	6175 ± 319	$(3.6 \pm 0.5) \times 10^{13}$	5285	H-mode
249	6060 ± 355	$(4.7 \pm 0.5) \times 10^{13}$	5644	H-mode
296	5968 ± 384	$(6.5 \pm 0.6) \times 10^{13}$	5432	H-mode

Table 1. Overview of experimental measurements.

of T_g for several axial positions are presented in *Wolf et al.* [2020] for slightly different conditions of input power and flow (860 W and 12 slm). They show, for L-mode conditions, an approximately flat distribution of T_g between 4000 and 2500 K within 5 mm from the axis, and in H-mode conditions, a temperature drop from 6000 K down to 2500 K in the same region. The peak power density in the center of the plasma P_{abs} is obtained, as described in *Wolf et al.* [2020], by normalization of the emission intensity profile to the total power input. The derivation is based on an Ohmic power deposition for which an implicit proportionality between emission intensity and electron density is assumed. In addition, this method assumes a Gaussian profile of emission intensity, electron density and absorbed power density and the spatial homogeneity of gas mixture composition and reduced electric field, even though the radial variations of these parameters may be relevant [*Groen et al.*, 2019]. Hence, the estimated values of peak power density are subjected to a large uncertainty for which we estimate an error bar of ± 50%.

The diameter $2R$ and length L of the plasma core are defined as the full-width at half maximum (FWHM) of the spontaneous emission intensity profiles in radial and axial direction, respectively, obtained from the O(3s^{5}S^0 ← 3p^{5}P) 777 nm triplet lines of atomic oxygen. The vortex flow induces convective and diffusive turbulent transport [*Chang and Dhir*, 1995]. This complexity severely complicates the accurate determination of transport in each location of the reactor. However, an average velocity v of the gas flowing through the plasma region of temperature T_g can be estimated through the mass conservation equation: $m_{CO_2} \cdot N_{in} \cdot \Gamma_{in} = \sum_i m_i n_i \cdot v \cdot S$, where m_{CO_2} is the mass of the CO_2 molecule, N_{in} is the number density of the input gas at pressure p and at 300 K according to the ideal gas law, Γ_{in} is the input flow of 18 slm, m_i and n_i are the mass and number density of each species i in the plasma core and S is the cross section of the quartz tube. In this way, a replacement time of plasma products by CO_2 in the plasma core $t_r = L/v$ is estimated. v and t_r in table 2 are calculated from the self-consistent simulation of steady-state composition, as described in section 3 and shown in section 4.2. Finally, the gas temperature and ionisation degree are represented as function of

p [mbar]	R [mm]	n_e/N_g [10^{-5}]	L [cm]	v [m s^{-1}]	t_r [ms]	Regime
60	7.28	0.61	1.38	109.21	0.126	Homogeneous
97	3.68	0.76	1.17	122.18	0.096	L-mode
108	1.78	1.85	1.21	151.01	0.080	Hybrid
121	1.74	6.03	1.54	163.28	0.094	Hybrid
141	1.77	12.0	1.89	159.47	0.119	Hybrid
161	1.84	9.72	2.25	142.83	0.158	H-mode
209	1.82	14.8	3.44	113.73	0.302	H-mode
249	1.75	15.7	3.46	94.52	0.366	H-mode
296	1.78	18.1	5.75	79.72	0.721	H-mode

Table 2. Overview of experimental measurements, calculated velocity v and replacement time t_r.

pressure in figure 2 to clearly show the dependence of these parameters on the discharge mode and structure. Vertical lines indicate the transitions between L-mode and hybrid regime and between hybrid regime and H-mode at 105 mbar and 150 mbar, respectively. In this work we focus on the transitions between the contracted modes and thus ignore the distinction between homogeneous mode and L-mode. It is visible in figure 2 that discharge contraction and the transition to H-mode are closely related to the increase in T_g to approximately 6000 K, which has been explained in *Wolf et al.* [2020] by the high heat capacity of the gas at this temperature. Moreover, it is interesting to notice that the ionisation degree increases from around 10^{-5} to 10^{-4} as the contraction mode changes and then increases proportionally to pressure in H-mode.
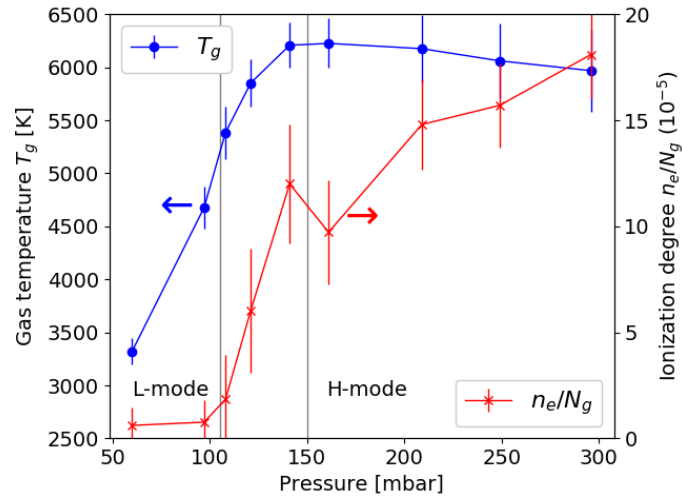
Figure 2. Experimentally measured gas temperature (left axis) and ionisation degree (right axis) as function of pressure. The vertical lines indicate the transitions between L-mode and hybrid regime and between hybrid regime and H-mode.

3. Zero-dimensional plasma chemistry model

Numerical simulations allow to assess parameters that are not experimentally measured and to obtain insights into plasma phenomena. Although we study phenomena in a non-uniform system, we assess the core of the CO_2 microwave plasma through a zero-dimensional model addressing the chemistry of the main neutral and charged particles in the plasma. The model investigates the experimental conditions described in the previous section. The core studied in the model is approximated as a volume in the plasma with maximum temperature, dissociation degree, absorbed power density (P_{abs}) and electron density (n_e). This model does not assess the plasma outside the core. We expect transport to remove plasma products from the core and to replace them by CO_2 in a timescale that we call t_r, self-consistently calculated following the mass conservation equation described in section 2. Other input parameters of the model are the experimental pressure and the measured T_g and n_e in the plasma core. Then, the model considers a total of 12 species: electrons, O^-, CO_2^+, CO^+, O_2^+, O^+, C^+, CO_2, CO, O_2, O and C. Apart from electron density, the density n_i of each species i is solved in time through the resolution of the particle rate equations:

$$\frac{dn_i}{dt} = S_i - L_i - \frac{n_i}{t_r} \ , \tag{1}$$

where S_i and L_i are the reaction rates of all sources and losses of species i, respectively, and $-\frac{n_i}{t_r}$ is the transport loss term. In the case of CO_2, an extra term $+\frac{\sum_i m_i n_i}{m_{CO_2} \cdot t_r}$ accounts for CO_2 replacement by transport on the right-hand side of eq. 1, following mass density conservation. The description of the reaction scheme considered and of electron kinetics is given in sections 3.1 and 3.2.

As dissociation of molecules takes place in this plasma and input T_g is constant in time, pressure is guaranteed to remain constant by normalizing every density n_i every time step such that the ideal gas law is preserved: $\sum n_i = p/(k_B T_g)$, where k_B is the Boltzmann constant. The set of ordinary differential equations (ODEs) is solved until reaching a stationary and quasi-neutral condition with the solver RADAU5, an implicit Runge-Kutta method of order 5 [*Hairer and Wanner*, 1996; *Hairer*, 2004]. This solver has been used in other zero-dimensional plasma chemistry models [*Obrusník et al.*, 2018; *Viegas et al.*, 2019; *Bílek et al.*, 2019]. Charged particle kinetics requires reduced electric field E/N_g, mean electron energy ϵ or electron temperature $T_e = \frac{2}{3}\epsilon$ as input parameters. These are iterated in time until the densities of ions match the input electron density, satisfying the quasineutrality criterion $|\frac{n_+ - n_- - n_e}{n_e}| < 10^{-9}$, where n_+ and n_- are the densities of positive and negative ions, respectively. The criterion for stationary condition is $max(|\frac{n_i(t) - n_i(t-\Delta t)}{n_i(t-\Delta t)}|) < 10^{-8}$, where Δt is the plasma chemistry time step. Finally, when quasineutrality and stationarity have been obtained, besides obtaining the steady-state E/N_g, ϵ, and n_i, we calculate the microwave power density absorbed by electrons in the core P_{abs} by solving the electron energy balance equation:

$$P_{abs} = \left(\frac{P_{el}}{N_g}(\epsilon, mix) + \frac{P_{inel}}{N_g}(\epsilon, mix) + \frac{P_{growth}}{N_g}(\epsilon, mix) \right) N_g \, n_e \ + \ \frac{n_e \epsilon}{t_r} \ , \tag{2}$$

where P_{el}, P_{inel} and P_{growth} are the components of power lost by electrons through elastic, conservative inelastic and non-conservative inelastic collisions, respectively, calculated from the solver for electron kinetics and dependent on gas mixture mix.

3.1. Reaction scheme

The reaction scheme used in the model is defined according to the following considerations:

- In the addressed conditions, the neutral composition of the CO_2 plasma core is expected to vary significantly. It is essential to accurately describe neutral thermal chemistry. We use the reactions in database GRI-MECH 3.0 [*Smith et al.*, 2018] for species CO_2, CO, O_2, O and C, presented in table 3. The rate coefficients for the reactions in this database have been obtained mostly from shock-tube measurements, in a wide range of pressure and temperature and including other species. We have confirmed that steady-state results using this reaction set approximately match thermodynamic results of Gibbs free energy minimization obtained through the calculator CEARUN [*Gordon and McBride*, 1994].

- Reactions involving species C_2, O_3 and C_2O from references [*Fairbairn*, 1969; *Husain and Kirsch*, 1971; *Slack*, 1976; *Baulch et al.*, 1976; *Hippler et al.*, 1990; *Beuthe and Chang*, 1997; *Fontijn et al.*, 2001; *Kwak et al.*, 2015; *Koelman et al.*, 2017] have also been considered. However, our simulation results in the conditions of relevance for this work have shown that these species are irrelevant for the description of the plasma and thus have been discarded.

- Table 3 only presents the rate coefficients of the foward reactions k_f. The rate coefficients of the reverse reactions k_r are calculated from k_f using the equilibrium constant as $k_r = N_g^\alpha k_f \exp(\Delta G / RT_g)$, where α is the difference between number of collision partners in reverse and forward reactions, R is the ideal gas constant, and ΔG is the change in Gibbs free energy of the reaction, calculated as $G_p - G_r$, where G_p and G_r are the Gibbs free energies of the products and reactants of the forward reaction, respectively. $G = H - S \times T_g$, where H is the enthalpy and S the entropy. $H/(RT_g)$ and S/R of each species can be found as polynomial functions of T_g in the GRI-MECH 3.0 database [*Smith et al.*, 2018].

- For forward reactions (N3-6), the database provides coefficients for the low-pressure limit assuming three bodies (k_0) and for the high-pressure limit assuming two bodies (k_∞). Then, following the recommendation of the database and the documentation of software CHEMKIN [*Kee et al.*, 2000], we use the Lindemann formula [*Lindemann*, 1922] to calculate the rate coefficient k:

$$k = k_\infty \frac{P_r}{1 + P_r} \; ; \; P_r = \frac{k_0 N_g}{k_\infty} \; . \tag{3}$$

- For charged particle kinetics, we base our reaction scheme on the one of *Koelman et al.* [2017], where the scheme of *Kozák and Bogaerts* [2014] has been reviewed. However, our simulation results in the conditions of relevance for the present work have shown that most ions are irrelevant for the description of the plasma. Then, we consider all the reactions in *Koelman et al.* [2017] for the relevant charged species: electrons, O^-, CO_2^+, CO^+, O_2^+, O^+ and C^+. These are presented in tables 4 and 5.

Nbr	Reaction	Forward rate coefficient
N1	$O + O + CO \leftrightarrow O_2 + CO$	$1.75 \times 3.31 \times 10^{-31} \times T_g^{-1}$
N2	$O + O + CO_2 \leftrightarrow O_2 + CO_2$	$3.60 \times 3.31 \times 10^{-31} \times T_g^{-1}$
N3	$O + CO + CO \leftrightarrow CO_2 + CO$	$1.5 \times 2.99 \times 10^{-14} \exp(-1195.27/T_g) \times \frac{P_r}{N_g(1+P_r)}$
N4	$O + CO + CO_2 \leftrightarrow CO_2 + CO_2$	$3.5 \times 2.99 \times 10^{-14} \exp(-1195.27/T_g) \times \frac{P_r}{N_g(1+P_r)}$
N5	$O + CO + O_2 \leftrightarrow CO_2 + O_2$	$6.0 \times 2.99 \times 10^{-14} \exp(-1195.27/T_g) \times \frac{P_r}{N_g(1+P_r)}$
N6	$O_2 + CO \leftrightarrow CO_2 + O$	$4.15 \times 10^{-12} \exp(-24021.37/T_g)$
N7	$CO + CO \leftrightarrow CO_2 + C$	$6.31 \times 10^{-11} \exp(-97013.83/T_g)$
N8	$CO + O \leftrightarrow C + O + O$	$0.5 \times 7.14 \times 10^3 \times T_g^{-3.1} \exp(-1288.10/T_g)$
N9	$CO + O_2 \leftrightarrow C + O + O_2$	$0.5 \times 7.14 \times 10^3 \times T_g^{-3.1} \exp(-1288.10/T_g)$
N10	$CO + CO \leftrightarrow C + O + CO$	$2.0 \times 7.14 \times 10^3 \times T_g^{-3.1} \exp(-1288.10/T_g)$
N11	$CO + CO_2 \leftrightarrow C + O + CO_2$	$1.0 \times 7.14 \times 10^3 \times T_g^{-3.1} \exp(-1288.10/T_g)$
N12	$O_2 + C \leftrightarrow CO + O$	$5.36 \times 10^{-12} \times T_g^{0.41} \exp(26.92/T_g)$

Table 3. List of neutral thermal chemistry reactions. The rate coefficients are provided for the forward reactions. The rate coefficients for the reverse reactions are calculated from the assumption of thermodynamic equilibrium. The units of rate coefficients for two-body reactions are cm^3 s^{-1} and for three-body reactions are cm^6 s^{-1}. N_g is the total gas density in cm^{-3} and T_g is the gas temperature in K.

- We assume that in conditions of steady-state and high T_g in the plasma core (3000 - 6500 K), electronically excited species have a negligible contribution to the main neutral and charged particle kinetics, and vibrational states of the molecular species are in thermal equilibrium with rotation and translation of molecules and atoms (as suggested by the temperature measurements in *van den Bekerom et al.* [2020]). As the neutral chemistry rate coefficients in use do not distinguish vibrational states, we assume they include the contribution of all states following a Boltzmann distribution function at temperature T_g. Furthermore, the rate coefficients for electron-impact reactions used in our chemistry model are calculated considering the contribution of vibrational states, as it will be explained in the next section. As a result, the contribution of vibrational states is included in the model, while keeping only 12 species and 81 reactions.

- Besides the electron-impact rate coefficients, whose calculation will be presented in the next section, for coherence purposes, the following rate coefficients have been chosen from a different source than in *Koelman et al.* [2017]: E20, E22, E23 and I22. Also, the following reactions have been added for completion of the scheme: I19, I20, I24, I25, I30, I31 and I32. Moreover, other coefficients have been tested for electron-ion recombination, ion transfer and detachment reactions. However, the effect these differences have on results is negligible.

- Finally, it should be noticed that the rate coefficients for associative ionisation of N+O and O+O are provided in *Park et al.* [1994], based on experimental data. Then, that work assumes the associative ionisation of C+O to take the same rate

Nbr	Reaction	Rate coefficient	Refs.
E1	$e + CO_2 \rightarrow CO_2^+ + 2e$	$k(\epsilon, mix)$	-
E2	$e + CO_2 \rightarrow CO + O^+ + 2e$	$k(\epsilon, mix)$	-
E3	$e + CO_2 \rightarrow O + CO^+ + 2e$	$k(\epsilon, mix)$	-
E4	$e + CO_2 \rightarrow O_2 + C^+ + 2e$	$k(\epsilon, mix)$	-
E5	$e + CO_2 \rightarrow C + O_2^+ + 2e$	$7 \times 10^{-13} T_e^{0.5}(1 + 1.3 \times 10^{-5} T_e)\exp(\frac{-1.5 \times 10^5}{T_e})$	[1]
E6	$e + CO \rightarrow CO^+ + 2e$	$k(\epsilon, mix)$	-
E7	$e + CO \rightarrow O + C^+ + 2e$	$k(\epsilon, mix)$	-
E8	$e + CO \rightarrow C + O^+ + 2e$	$k(\epsilon, mix)$	-
E9	$e + O_2 \rightarrow O_2^+ + 2e$	$k(\epsilon, mix)$	-
E10	$e + O_2 \rightarrow O + O^+ + 2e$	$k(\epsilon, mix)$	-
E11	$e + O \rightarrow O^+ + 2e$	$k(\epsilon, mix)$	-
E12	$e + C \rightarrow C^+ + 2e$	$k(\epsilon, mix)$	-
E13	$e + CO_2 \rightarrow CO + O^-$	$k(\epsilon, mix)$	-
E14	$e + CO \rightarrow C + O^-$	$k(\epsilon, mix)$	-
E15	$e + O_2 \rightarrow O + O^-$	$k(\epsilon, mix)$	-
E16	$e + O + M \rightarrow O^- + M$	10^{-31}	[2,3]
E17	$e + CO_2 \rightarrow e + CO + O$	$k(\epsilon, mix)$	-
E18	$e + CO \rightarrow e + C + O$	$k(\epsilon, mix)$	-
E19	$e + O_2 \rightarrow e + O + O$	$k(\epsilon, mix)$	-
E20	$e + CO_2^+ \rightarrow CO + O$	$3.94 \times 10^{-7} \times T_e^{-0.4}$	[1]
E21	$e + CO_2^+ \rightarrow C + O_2$	$3.94 \times 10^{-7} \times T_e^{-0.4}$	[1]
E22	$e + CO^+ \rightarrow C + O$	$3.46 \times 10^{-8} \times T_e^{-0.48}$	[4,5,6]
E23	$e + O_2^+ + M \rightarrow O + O + M$	$1.61 \times 10^{-27} \times T_e^{-0.5}$	[1]
E24	$e + O_2^+ \rightarrow O + O$	$6.0 \times 10^{-7} \times T_e^{-0.5} \times T_g^{-0.5}$	[2,3]
E25	$e + O^+ + M \rightarrow O + M$	$2.49 \times 10^{-29} \times T_e^{-1.5}$	[7]

Table 4. List of charged particle reactions: electron-impact ionisation, attachment and dissociation; electron-ion recombination. The units of rate coefficients for two-body reactions are cm^3 s^{-1} and for three-body reactions are cm^6 s^{-1}. ϵ is the mean electron energy, mix is the gas mixture, T_e is the electron temperature in K for reaction E5 and in eV for the remaining reactions, M represents any neutral species, and T_g is the gas temperature in K. References: [1] = *Beuthe and Chang* [1997]; [2] = *Cenian et al.* [1994]; [3] = *Hokazono and Fujimoto* [1987]; [4] = *Berthelot and Bogaerts* [2018]; [5] = *Mitchell and Hus* [1985]; [6] = UMIST database [*Mcelroy et al.*, 2013]; [7] = *Kossyi et al.* [1992].

coefficient as N+O, which at 6000 K is three orders of magnitude higher than the one for O+O. In this work, as associative ionisation is not expected to be the dominant ionisation process, we take the rate coefficient of O+O associative ionisation for the three associative ionisation processes (I30-32).

Nbr	Reaction	Rate coefficient	Refs.
I1	$CO_2 + O^+ \rightarrow CO + O_2^+$	8.1×10^{-10}	[1,8]
I2	$CO_2 + O^+ \rightarrow O + CO_2^+$	9.0×10^{-11}	[1,8]
I3	$CO_2 + C^+ \rightarrow CO + CO^+$	1.1×10^{-9}	[1,8]
I4	$CO_2 + CO^+ \rightarrow CO + CO_2^+$	1.0×10^{-9}	[1,2,3,8]
I5	$CO + O^+ \rightarrow O + CO^+$	$2.83 \times 10^{-13} \times T_g^{0.5} \exp(-4580/T_g)$	[8]
I6	$CO + C^+ \rightarrow C + CO^+$	5.0×10^{-13}	[1,8]
I7	$C + CO^+ \rightarrow CO + C^+$	1.1×10^{-10}	[6]
I8	$C + O_2^+ \rightarrow O + CO^+$	5.2×10^{-11}	[6]
I9	$C + O_2^+ \rightarrow O_2 + C^+$	5.2×10^{-11}	[6]
I10	$O + CO_2^+ \rightarrow CO + O_2^+$	1.64×10^{-10}	[6]
I11	$O + CO_2^+ \rightarrow CO_2 + O^+$	9.62×10^{-11}	[6]
I12	$O_2 + CO_2^+ \rightarrow CO_2 + O_2^+$	5.3×10^{-11}	[6]
I13	$O + CO^+ \rightarrow CO + O^+$	1.4×10^{-10}	[1,6,8]
I14	$O_2 + CO^+ \rightarrow CO + O_2^+$	1.2×10^{-10}	[1,6,8]
I15	$O_2 + C^+ \rightarrow CO + O^+$	4.54×10^{-10}	[6]
I16	$O_2 + C^+ \rightarrow O + CO^+$	3.8×10^{-10}	[1,8]
I17	$O_2 + O^+ \rightarrow O + O_2^+$	$3.29 \times 10^{-10} \times T_g^{-0.5}$	[1,8]
I18	$O + O^+ + M \rightarrow O_2^+ + M$	1.0×10^{-29}	[7]
I19	$O + O_2^+ \rightarrow O_2 + O^+$	$6.64 \times 10^{-12} \times T_g^{-0.09} \exp(-18000/T_g)$	[9]
I20	$O_2 + C^+ \rightarrow C + O_2^+$	$1.66 \times 10^{-11} \exp(-9400/T_g)$	[9]
I21	$CO + O^- \rightarrow CO_2 + e$	5.5×10^{-10}	[1,8]
I22	$O + O^- \rightarrow O_2 + e$	1.3×10^{-9}	[10]
I23	$M + O^- \rightarrow M + O + e$	4.0×10^{-12}	[2,3]
I24	$C + O^- \rightarrow CO + e$	5.0×10^{-10}	[6]
I25	$O_2 + O^- \rightarrow O_2 + O + e$	6.9×10^{-10}	[1]
I26	$O^+ + O^- \rightarrow O + O$	$4.65 \times 10^{-7} \times T_g^{-0.43}$	[11]
I27	$O^+ + O^- + M \rightarrow O_2 + M$	$1.56 \times 10^{-19} \times T_g^{-2.5}$	[1]
I28	$O_2^+ + O^- \rightarrow O_2 + O$	$3.20 \times 10^{-7} \times T_g^{-0.44}$	[11]
I29	$O_2^+ + O^- \rightarrow O + O + O$	$5.17 \times 10^{-6} \times T_g^{-0.44}$	[11]
I30	$O + O \rightarrow O_2^+ + e$	$1.18 \times 10^{-21} \times T_g^{2.7} \exp(-80600/T_g)$	[9]
I31	$C + O \rightarrow CO^+ + e$	$1.18 \times 10^{-21} \times T_g^{2.7} \exp(-80600/T_g)$	(I30)
I32	$CO + O \rightarrow CO_2^+ + e$	$1.18 \times 10^{-21} \times T_g^{2.7} \exp(-80600/T_g)$	(I30)

Table 5. List of charged particle reactions: ion transfers, detachment, ion-ion recombination and associative ionisation. The units of rate coefficients for two-body reactions are cm^3 s^{-1} and for three-body reactions are cm^6 s^{-1}. M represents any neutral species and T_g is the gas temperature in K. References: [1] = *Beuthe and Chang* [1997]; [2] = *Cenian et al.* [1994]; [3] = *Hokazono and Fujimoto* [1987]; [6] = UMIST database [*Mcelroy et al.*, 2013]; [7] = *Kossyi et al.* [1992]; [8] = *Albritton* [1978]; [9] = *Park et al.* [1994]; [10] = *Guerra et al.* [2019]; [11] = *Gudmundsson and Thorsteinsson* [2007].

3.2. Electron kinetics

The power loss terms in eq. 2 and the electron-impact rate coefficients in table 4 are determined from electron kinetics calculations using the Monte Carlo Flux (MCF) method, that has been introduced in *Schaefer and Hui* [1990]. Recently, an improved version of MCF has been implemented by some of the present authors and benchmarked against two-term and multi-term solutions of the electron Boltzmann equation [*Vialetto et al.*, 2019]. This method allows one to overcome the limitations of commonly-used two-term solvers with much faster calculations than in a conventional Monte Carlo approach. However, to the best of our knowledge, no other works are found using MCF to couple electron and chemical kinetics in a plasma. In this work, MCF is applied to different gas mixtures and discharge parameters. Moreover, here we extend the method for calculations in fields at high frequencies that are typical of MW discharges. For this purpose, a time dependent electric field has been implemented within the MCF solver in the form of:

$$\mathbf{E}(t) = E_0 \cos\left(\omega t\right) \mathbf{e_z} \ , \tag{4}$$

where $\mathbf{E}(t)$ is the electric field at time t, E_0 is the amplitude of the field, ω is the angular frequency and $\mathbf{e_z}$ is the versor along the direction of $\mathbf{E}$. The modified time step technique [*Longo*, 2006] has been implemented to calculate transition probabilities between energy space cells. Details about this method for the description of electron kinetics in oscillating fields will be presented elsewhere.

As input parameters for the electron kinetics calculations, we consider gas pressure, gas temperature and frequency of the field ($f = \omega/2\pi$), consistently with the plasma chemistry model and the experimental conditions reported in section 2, as well as an initial guess for gas composition. Cross sections of electron-impact processes are taken from the LXCat databases [*Pancheshnyi et al.*, 2012]. In this work, the following is considered:

- CO_2 electron kinetics is described using the cross sections included in the Biagi database [*Biagi*, 2019]. Details about application of MCF for studies of electron kinetics in CO_2 with the same dataset of cross sections will be presented in a separate paper [*Vialetto et al.*]. It is worth noting that those cross sections have been transcribed from the source code Magboltz (version 8.9 and later) [*MAGBOLTZ*, 2019] and are suitable for use in Monte Carlo and multi-term Boltzmann solvers for comparison with swarm analysis experiments. We assume that cross sections for electronic excitation, ionisation and dissociation are the same from all the vibrationally excited states of the ground electronic state (i.e. $CO_2(X)$). Moreover, since the elastic momentum transfer cross sections of CO_2 take into account contributions of the ground vibrational state (i.e. $CO_2(X, \nu_1\nu_2\nu_3 = 000)$, $\nu_{1,2,3}$ being the vibrational quantum numbers of the symmetric stretching, bending and asymmetric stretching modes, respectively), vibrational bending mode and rotational levels in thermal equilibrium at 293.15 K, those cross sections are modified to take into account the population of the vibrational bending mode

levels at different gas temperatures, as it will be described in a separate paper [*Vialetto et al.*]. Superelastic cross sections from low-lying vibrational states (i.e. $CO_2(X, 010)$, $CO_2(X, 020)$, $CO_2(X, 100)$, $CO_2(X, 030 + 110)$ and $CO_2(X, 001)$) are also included and calculated with the formula of Klein-Rosseland [*Capitelli et al.*, 2015], by considering micro-reversibility.

- CO electron kinetics is described using the IST-Lisbon dataset of cross sections that has recently been uploaded to LXCat [*Alves*, 2014; *Ogloblina et al.*, 2020]. The applicability of those cross sections has been checked by comparing Monte Carlo calculations with two-term solutions of the electron Boltzmann equation obtained with the solver LoKI-B [*Tejero-del Caz et al.*, 2019] in pure CO (not shown here). In our calculations, we assume that electron-impact electronic excitation, dissociation and ionisation take place from the ground electronic state. The first 11 lowest lying vibrational levels of the ground electronic state are taken into account (i.e. $CO(X, \nu = 0 - 10)$) in vibrational excitation/de-excitation processes. In addition, rotational excitation and de-excitation processes ($CO(X, \nu = 0, J = 0 - 17)$) are taken into account. The total ionisation cross sections of CO are replaced with the ionisation cross sections of the Itikawa database [*Itikawa*, 2015], that reproduce the same total ionisation cross sections. This choice has been preferred in order to take into account production of different ions.

- O_2 electron kinetics is considered using the IST-Lisbon dataset of cross sections [*Alves et al.*, 2016]. The same procedure described for ionisation of CO has been applied to O_2.

- Electron-impact cross sections with O atoms and C atoms are taken from the IST-Lisbon and BSR databases [*Alves et al.*, 2016; *Zatsarinny and Bartschat*, 2004], respectively.

The importance of considering the vibrational populations in CO_2 plasma at high T_g for calculation of the EEDF and the electron-impact rate coefficients has been noticed in *Wang and Bogaerts* [2016]. In this work, we assume that those states are populated according to a Boltzmann distribution at T_g. Then, for a given gas composition, 21 values of reduced electric field (E/N_g, where E is the root mean square of the field, $E = \frac{E_0}{\sqrt{2}}$) linearly spaced between 10 and 100 Td are considered as input for the solution of the Boltzmann problem. As output, EEDFs, rate coefficients of electron-impact processes, swarm parameters, electron mean energy ϵ and electron power losses are calculated. Such quantities are interpolated as a function of ϵ and used as input in the plasma chemistry model. Since the change of gas composition computed by the chemistry model affects, in turn, the electron kinetics, the MCF calculations are updated for a correct calculation of electron kinetics. As a compromise between accuracy and computational time, MCF calculations are updated when the density of one of the main species (species with molar fraction above 2%) changes by 10% with respect to the previous guessed composition. In this way, the electron kinetics is coupled self-consistently with the chemical kinetics and allows one to take into account the gas

composition. On average, the composition is updated two times during a simulation run (each run corresponding to one experimental condition) and thus all the quantities related to electron kinetics are computed three times per run. The computational time for the simulation of 21 values of E/N_{g} is approximately 20 minutes, which brings the average computational time per run to about 1 hour. Despite the longer computational time that the coupling between plasma chemistry and electron kinetics requires with composition update, this approach is preferred to others (e.g. tabulation of electron parameters for a set of fixed compositions) when composition is variable within a wide range and the electron kinetics solution is highly dependent on the gas composition, as it is the case in the system under study.

4. Results

4.1. Comparison between numerical and experimental peak power density

The power density absorbed by electrons in the core P_{abs}, obtained from the simulations for the set of 9 conditions described in tables 1 and 2, and calculated through eq. 2, is compared to the peak P_{abs} estimated in experiments in figure 3. The experimental estimation of P_{abs} assumes an error bar of $\pm$ 50%, as described in section 2. In the simulation results, the points indicate the result taking the measured n_e and T_g from table 1 as input and t_r calculated as in table 2. The error bars in the simulation results represent the range of possible outputs within the uncertainties of the input parameters: error bar in n_e ($\pm\delta_{n_e}$) and T_g ($\pm\delta_{T_g}$) measurements and uncertainty in replacement time t_r with minimum 0.1 ms or the standard value and maximum 10 ms. The maxima P_{abs} are obtained when the following inputs are considered: $n_e + \delta_{n_e}$, $T_g - \delta_{T_g}$ and minima t_r. Conversely, the minima P_{abs} are calculated when taking $n_e - \delta_{n_e}$, $T_g + \delta_{T_g}$ and $t_r = 10$ ms. The effect of the uncertainty of each input parameter (t_r, T_g and n_e) separately on the simulation results is analysed in section 4.5.
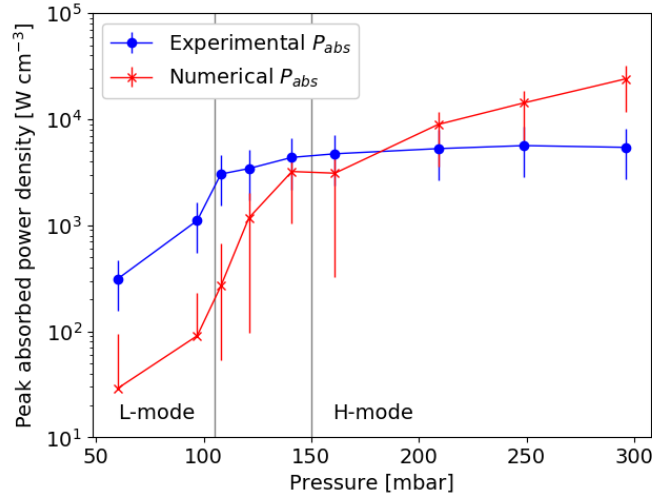

Figure 3. Peak absorbed power density from experiments and simulations, as function of pressure. The vertical lines indicate the discharge mode transitions.

The model results in figure 3 tendentiously indicate that to reach the measured electron densities, lower P_{abs} than measured are required in L-mode and hybrid regimes and higher P_{abs} than measured are required in H-mode. Moreover, the simulation results suggest that n_e and P_{abs} increase almost in the same proportion in the whole parameter range, as is expected according to eq. 2. In fact, in H-mode, from 161 mbar to 296 mbar, numerical P_{abs} (using standard input) increases from 3.1 to 24.0 kW cm^{-3}, a factor 7.7. In the same range, n_e increases by a factor 3.6 and N_g by a factor 1.9. According to eq. 2, neglecting electron energy transport losses, this result is expected with relatively small variations of ϵ and mix with pressure in H-mode. Conversely, experimental results suggest a proportionality between n_e and P_{abs} to be present only up to 161 mbar. Then,

experiments indicate that both peak n_e and ionisation degree increase with pressure in H-mode without significant increase in peak T_g and P_{abs} (see figure 2). According to eq. 2, this would imply a decrease in ϵ with pressure, which in turn would decrease ionisation through electron-impact, a significant change of mixture, or a more important increase of t_r with pressure. None of these conditions seems likely.

We attribute the discrepancies to limitations in the P_{abs} estimations in both experiments and simulations. On the one hand, the method to estimate peak power density in experiments is subject to several assumptions, as has been described in section 2. On the other hand, the zero-dimensional model relates only local parameters, while in reality the peak electron density may be related also to parameters in the surrounding environment, as suggested by the results in *Groen et al.* [2019]. In that work the location of the peak of the simulated reduced electric field is different than the location of the core where the peak of the input n_e is placed. That limitation is translated in the errorbar that includes the uncertainty in the reduced electric field in the core, as shown in section 4.5. Furthermore, the model assumes a reaction scheme and a set of rate coefficients that are also subjected to uncertainty. The discrepancy between numerical and experimental results could indicate the presence in experiments of processes that are not taken into account in the model: electron-production processes whose rate increases with pressure and/or electron losses whose rate is independent of or decreases with pressure. This assessment has led us to test in the model the higher C+O associative ionisation rate coefficient presented in *Park et al.* [1994] and *Sun et al.* [2017]. However, this higher rate would lead to $P_{abs} \sim 10$ W cm^{-3} when $T_g \sim 6000$ K and therefore has been discarded.

Finally, we conclude that, despite limitations, figure 3 presents a qualitative agreement between numerical and experimental results and shows that the model can describe the main processes taking place in the plasma core. Indeed, the transition between a more diffusive L-mode with peak power density of the order of hundreds W cm^{-3} towards a more contracted H-mode with P_{abs} of the order of thousands W cm^{-3} is present in both numerical and experimental results. Moreover, the uncertainty presented in the numerically-obtained P_{abs} almost accounts for the difference with respect to the experimental P_{abs}. This result shows the sensitivity of the model to the uncertainty in input parameters, the importance of taking it into account when analysing simulation results and comparing them with experiments and the importance of accurate measurements and accurate estimation of turbulent transport effects.

4.2. Neutral composition in plasma core

As the model qualitatively describes P_{abs} in the plasma core, we use it to assess other plasma parameters. In this section, the neutral composition in the plasma core is evaluated through simulation results. The left side of figure 4 shows the relative densities of the most important neutral species in the plasma core taking into account only neutral thermal chemistry (table 3) and also charged particle kinetics, for the set of 9 experimental conditions. These are represented only using the input of tables 1 and 2, without taking uncertainties into account. Yet, neutral composition is also dependent on the uncertainty in input parameters, as higher dissociation (both of CO_2 and of CO) is obtained with $T_g + \delta_{T_g}$, $n_e + \delta_{n_e}$ and $t_r = 10$ ms. For instance, the CO relative density can vary between 1 and 45% at 60 mbar and between 44% and 50% in H-mode. The effect of the uncertainty of each input parameter is evaluated in section 4.5, always including charged particle kinetics. Then, on the right side of figure 4, the standard result with charged particle kinetics is compared to the result of thermal equilibrium, i.e. without charged particles and with $t_r = \infty$.
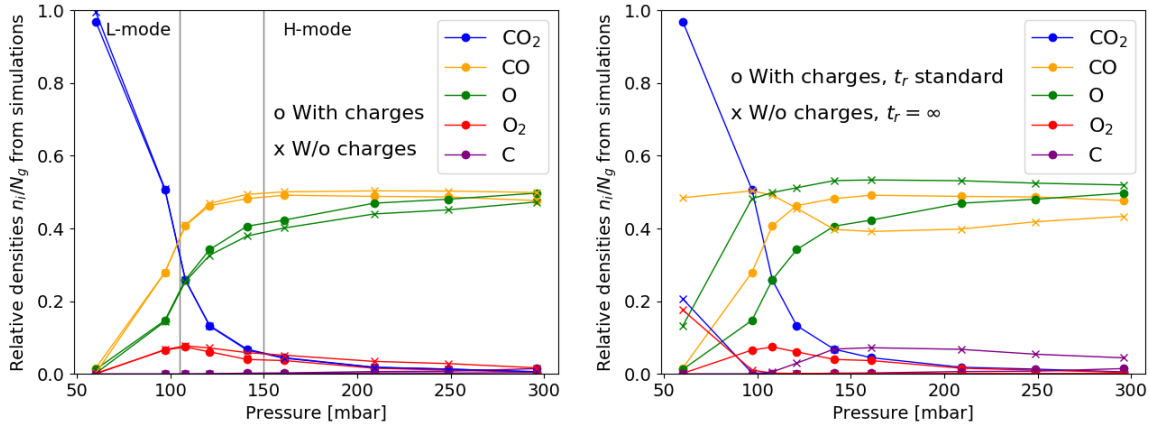

Figure 4. Relative densities of neutral species as a function of pressure from the simulations: On the left, with standard t_r, with and without charged particle kinetics (the vertical lines indicate the discharge mode transitions). On the right, with charged particles and standard t_r and the case of thermal equilibrium with $t_r = \infty$.

Figure 4 shows that the mode transition is accompanied by a transition in neutral composition. This is expected, since a change in neutral composition is directly linked to heat exchange [*Zhong et al.*, 2019; *Wolf et al.*, 2020], and because neutral composition has a large influence on charged particle kinetics, as will be shown. While the homogeneous mode ($p = 60$ mbar, $T_g = 3322$ K) is characterised by a large amount of CO_2, with possibly some relevant CO and O_2 densities, the H-mode ($p \geq 161$ mbar, $T_g \geq 6000$ K) corresponds to a completely dissociated plasma core, composed mostly of CO and O, with possibly some relevant amount of C, in agreement with the assumptions in *den Harder et al.* [2017]; *van den Bekerom et al.* [2019]; *Groen et al.* [2019]; *Wolf et al.* [2019, 2020]. The simulation results suggest that the core of the L-mode and hybrid regime plasmas ($p = 97 - 141$ mbar, $T_g \simeq 4000 - 6000$ K) is composed of a progressively

dissociated mixture of CO_2, CO, O_2 and O. This is the parameter-range pointed as most favourable for efficient plasma-driven conversion of CO_2 in *Wolf et al.* [2020]. The results in figure 4, together with the uncertainties in section 4.5, also show that the neutral composition in the plasma core is not only determined by the local equilibrium of thermal chemistry, but also by transport processes and by charged particle kinetics. Indeed, it is visible that the plasma in thermal equilibrium ($t_r = \infty$) would be significantly more dissociated than in the case where transport processes are considered. The reaction rates of the most relevant CO_2 dissociation processes are represented in figure 5.
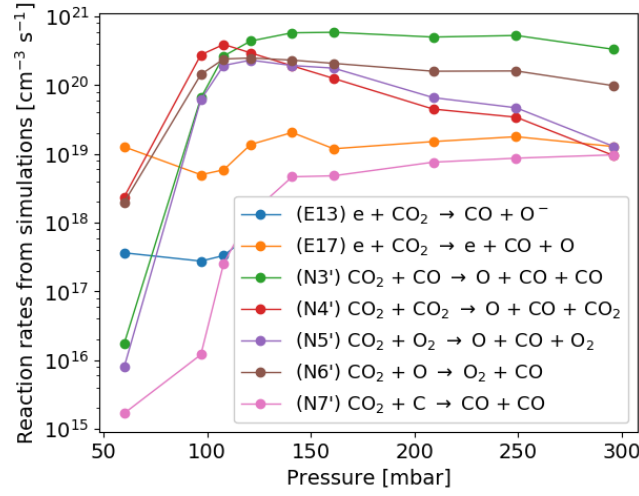
Figure 5. Reaction rates of the most important reactions of CO_2 dissociation in the plasma core as a function of pressure, from the simulations with standard parameters.

At 60 mbar and 3322 K, CO_2 is dissociated mostly through electron-impact dissociation (E17) with some relevant contribution from thermal reactions (N4', reverse reaction of N4) and (N6'). On the other hand, CO_2 at 60 mbar is mostly reintroduced by fast transport ($t_r = 0.13$ ms, rate $\sim 10^{21}$ cm^{-3}s^{-1}). Then, in L-mode and in hybrid regime, CO_2 collisions with any neutral are relevant for dissociation, along with their reverse processes and transport losses. Finally, in H-mode, besides transport, CO_2 dissociation through collisions with CO and O (N3' and N6') and dissociation of CO (N12') become dominant processes, along with their reverse reactions, with rates above 10^{19} cm^{-3}s^{-1}. Electron-impact dissociation of CO and O_2 (E18-E19) and dissociative attachment of CO (E14) have a small influence on the neutral composition in H-mode, leading to a more atomic (O and C) and less molecular (O_2 and CO) plasma. However, figure 4 shows that the differences in neutral composition with and without charged particle kinetics are subtle and lie within the uncertainties shown in section 4.5. Contrarily to the results in *Pietanza et al.* [2020], numerically assessing a very similar plasma (input flow rate 6 slm instead of 18 slm) at 250 mbar, here we conclude that the plasma core in H-mode, with $T_g \simeq 6000$ K, is mostly composed of CO and O, and this composition is defined by neutral thermal chemistry and transport processes. This conclusion is not affected by the evaluation of uncertainties presented in section 4.5.

4.3. Ionisation degree in plasma core

In this section, we analyse the phenomena leading to the change in ionisation degree associated with the mode transition. First, the ion composition in the plasma core is presented in figure 6. This figure shows the densities of electrons and positive ions, using the input parameters from tables 1 and 2, without considering the uncertainties exposed in section 4.5.
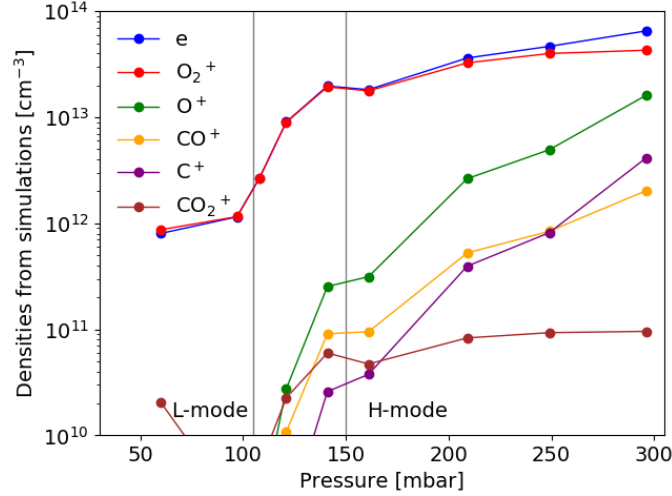

Figure 6. Ion composition: number densities of electrons and positive ions as function of pressure, from the simulations. The vertical lines indicate the discharge mode transitions.

Figure 6 shows that the density of the dominant ion O_2^+ is approximately equal to n_e in homogeneous mode, in L-mode and in hybrid regime, while in H-mode its relative density decreases with pressure, accompanied by an increase of the densities of atomic ions O^+ and C^+. O_2^+ has also been found to be the dominant ion in a wide temperature range in *Wang et al.* [2016], where only CO_2^+ and O_2^+ positive ions have been considered. In fact, the ion composition is strongly dependent on the neutral composition and thus on gas temperature. It is also shown to be highly dependent on transport in section 4.5, due to its influence on neutral composition, as a possible higher t_r leads to a more atomic ion composition in hybrid regime and in H-mode. The transition of dominant ion with temperature has also been noticed in argon plasmas in *Martinez et al.* [2004]; *Dyatko et al.* [2008]; *Ridenti et al.* [2018]. O_2^+ is the dominant ion when the plasma is mostly molecular and the atomic ion densities increase when the neutral composition shifts to O/CO/C. It should be noticed that the density of negative ion O^- is always below 10^{11} cm^{-3} and ion-ion recombination reactions have a negligible role. Although attachment and detachment rates are high (above 10^{18} cm^{-3} s^{-1}), they almost compensate each other and only have a role at 60 mbar and 3322 K, as already noticed in *Wang and Bogaerts* [2016]. This result agrees with the assessment in *Fridman and Kennedy* [2004] stating that CO_2 discharges are controlled by electron-ion recombination since CO molar fractions above 10^{-3} guarantee effective detachment. Thus, the ion composition

is determined by electron-impact ionisation, associative ionisation, recombination and ionic conversion. It is worth noticing that all these charged-particle processes have μs characteristic times, while neutral chemistry (ms timescale in L-mode and μs timescale in H-mode) and transport losses (ms timescale) are slower processes. Indeed, the transport losses of charged particles have rates only up to 10^{17} cm^{-3}s^{-1} at high pressures, and below 10^{16} cm^{-3}s^{-1} at 60 and 97 mbar. The rates of the most important ionisation and recombination reactions are presented in figure 7. At 60 mbar, electron-impact ionisation of CO_2 is the main production channel. Then, ionic conversion reactions (mainly $CO_2^+ \rightarrow O_2^+$, $CO_2^+ \rightarrow O^+$ and $O^+ \rightarrow O_2^+$) determine O_2^+ as dominant ion. As the neutral composition changes, electron-impact ionisation of O, CO and C become increasingly important in H-mode. Although increasing with p and T_{g}, associative ionisation (I30-I32) is never a dominant process. The transition from O_2^+ to atomic ions with pressure is the result of dissociative recombination of CO_2^+, CO^+ and O_2^+, together with ion transfers (the dominant ones being $CO^+ \rightarrow O^+$, $O^+ \rightarrow O_2^+$ and $O_2^+ \rightarrow C^+$). Indeed, according to the ionisation potential of each species, ionic conversion tendentiously leads to the following sequence (ionisation thresholds in eV in brackets):

$$CO^+(14.0) \rightarrow CO_2^+(13.8) \rightarrow O^+(13.6) \rightarrow O_2^+(12.1) \rightarrow C^+(11.2) \qquad (5)$$
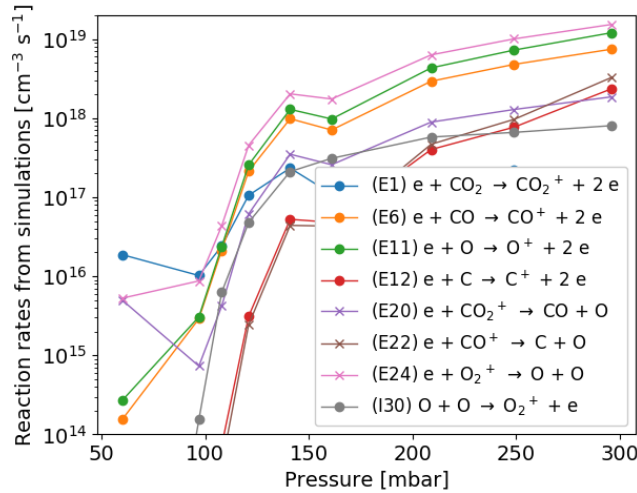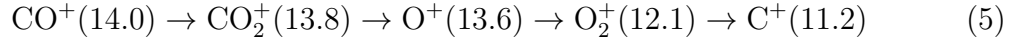

Figure 7. Reaction rates of the main ionisation (circles) and recombination (crosses) mechanisms, from the simulations.

As in *Martinez et al.* [2004]; *Ridenti et al.* [2018], at high pressures, even when the dominant positive ion is atomic, electron-ion recombination losses are dominant over losses of charged particles by transport. As electron losses mostly take place through dissociative recombination of molecular ions, the results of figures 6 and 7 show the importance of ion composition for the ionisation degree in the plasma core and its relationship with mean electron energy and peak power density. On the other hand, electron production is also dependent on the gas mixture. Figure 8 presents, on the left, the main electron-impact ionisation rate coefficients for a large range of ϵ,

obtained from the EEDF solutions with MCF in a 50% CO - 50% O mixture, a relevant mixture in H-mode. It is visible that the ionisation coefficient of C is significantly higher for the whole range of ϵ, which justifies the impact of this reaction on charge balance even when C fraction remains below 10%. On the right hand side of figure 8, the effective electron-impact ionisation rate coefficients are represented for different possible mixtures in the plasma core of the CO_2 conversion reactor: pure CO_2, partially dissociated CO_2 (30% CO_2, 40% CO, 20% O, 10% O_2), fully dissociated CO_2 (50% CO, 50% O) and partially dissociated CO (38% CO, 54% O, 8% C). For the case in pure CO_2, the ionisation coefficient is compared with the one obtained using the two-term solver Bolsig+ [*Hagelaar and Pitchford*, 2005] and the cross sections of the Biagi database [*Biagi*, 2019] in LXCat. The effective coefficients are calculated from the EEDF solutions for each corresponding mixture, using the fractions χ_i and the main electron-impact ionisation coefficients k_i of each species i:

$$k_{\text{eff}} = \chi_{CO_2} k_{CO_2} + \chi_{CO} k_{CO} + \chi_{O_2} k_{O_2} + \chi_O k_O + \chi_C k_C \tag{6}$$
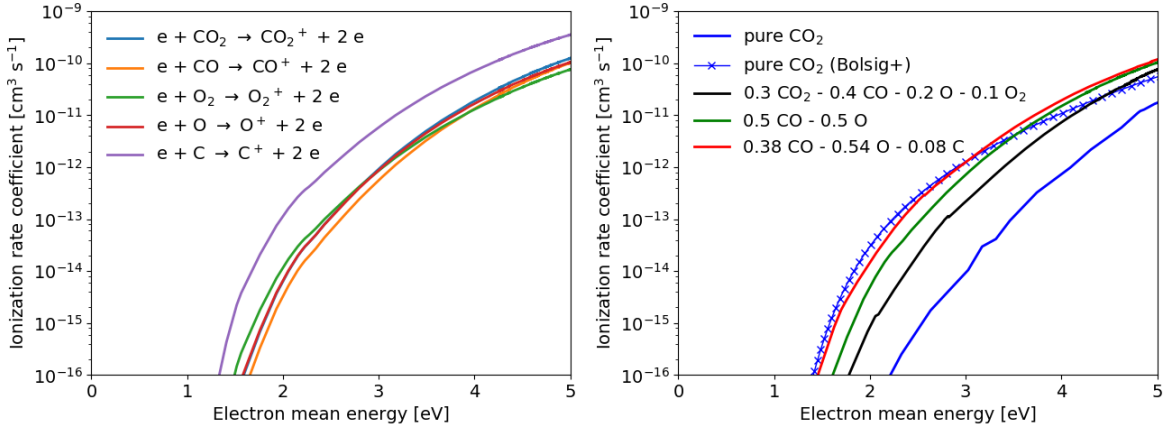

Figure 8. On the left, rate coefficients of the main electron-impact ionisation reactions as function of ϵ, from EEDF solutions in a 50% CO - 50% O mixture. On the right, effective ionisation rate coefficients as function of ϵ for 4 different mixtures, from the corresponding EEDF solutions. In every calculation, $T_g = 6000$ K, $p = 200$ mbar and $f = 2.45$ GHz.

Firstly, it is interesting to notice that the ionisation coefficient in pure CO_2 varies significantly with the different solvers, revealing the importance of the treatment of electron kinetics. The differences between the MCF and Bolsig+ results, that exceed the discrepancies expected from the two-term approximation [*Braglia and Romanò*, 1984; *Vialetto et al.*], are mostly due to the different treatment of the excited states population at high temperature. In fact, in MCF, the states are populated according to a Boltzmann distribution at gas temperature, with calculated statistical weights, and the elastic momentum transfer cross section is modified by considering the population of bending mode levels. That is not the case in Bolsig+, as it assumes the statistical weight of every state to be 1 and does not modify the elastic momentum transfer cross section according to the population at high temperature.

Then, figure 8 shows that electron-impact ionisation increases with the degree of dissociation in the plasma. Indeed, for the same electron mean energy, the ionisation rate coefficient is higher in a mixture with C than in a case without CO dissociation. It is also higher in a plasma where O_2 is fully dissociated than in a plasma containing this species. Besides the significantly higher ionisation rate coefficient of atomic carbon, this effect is due to the higher electron energy losses in molecular gases, that determine that the EEDF tends to have a higher tail in more atomic plasmas, as shown in *Wang and Bogaerts* [2016]. Hence, we can conclude that the transition in neutral composition contributes to the increase of n_e and n_e/N_g associated to discharge contraction. However, figure 8 also shows a strong dependence of electron-impact ionisation on the electron mean energy. This parameter is shown as a simulation result on the left side of figure 9, along with E/N_g, with standard input parameters from tables 1 and 2. We should again notice that E/N_g is defined as $\frac{E_0/N_g}{\sqrt{2}}$, E_0 being the amplitude of the MW field, interpolated between the different runs of the electron kinetics solver. Section 4.5 shows the effect of the uncertainties in t_r, T_g and n_e on the simulated ϵ and E/N_g. On the right side of figure 9 are represented the most important rate coefficients for charge balance (effective electron-impact ionisation k_{eff} and dissociative recombination k_{rec} of CO_2^+, O_2^+ and CO^+), as well as the ratio between them, for the set of 9 conditions.
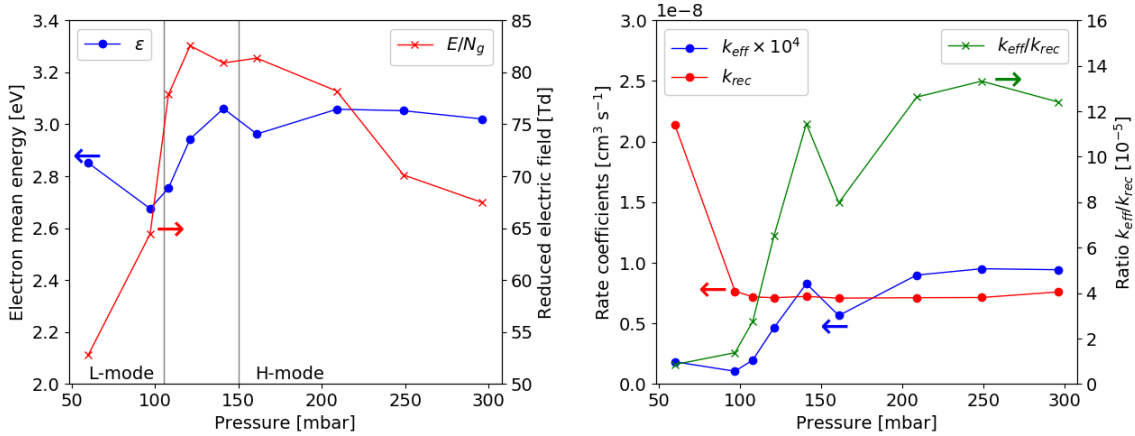

Figure 9. On the left, electron mean energy ϵ and reduced electric field E/N_g from the simulations. The vertical lines indicate the discharge mode transitions. On the right, effective electron-impact ionisation and recombination coefficients and the ratio between them.

It is shown in figure 9 that ϵ remains between 2.6 and 3.1 eV and E/N_g stays between 50 and 85 Td. However, the parameteric study in section 4.5 shows large uncertainties of these parameters, which also reflects limitations in the dimensionality of the model. Regardless of the large uncertainties, it is interesting to notice that the mode transition also appears to be present in the simulation results of ϵ. Indeed, with the sharp variation of T_g, composition and n_e in L-mode and hybrid regime, ϵ increases from around 2.6 to about 3.0 eV, with standard input conditions, which agrees with the tendencies in *Martinez et al.* [2004]; *Shneider et al.* [2012]; *Ridenti et al.* [2018]; *Zhong*

et al. [2019]. Then, in H-mode, ϵ appears to have only small variations with pressure. Conversely, E/N_g firstly increases with pressure but then decreases in H-mode as the molar fractions of O and C increase. The correspondence between E/N_g and ϵ shows a strong dependence of the local gas mixture. The values of ϵ and E/N_g in figure 9 are generally different than those in *Groen et al.* [2019], *Wolf et al.* [2019] and *Pietanza et al.* [2020] in similar conditions, obtained using two-term solvers for electron kinetics. However, most of the differences fall within the error bars presented in section 4.5, once again showing the importance of taking the uncertainties in input parameters into account.

It is interesting to notice that we can write the electron particle balance as function of n_e, gas density N_g, molecular ion density (CO_2^+, O_2^+ and CO^+) n_{MI}, k_{eff} and k_{rec} as:

$$n_e N_g k_{eff}(\epsilon, mix) = n_e n_{MI} k_{rec}(\epsilon) \tag{7}$$

$$\frac{n_e}{N_g} = \frac{n_e}{n_{MI}} \frac{k_{eff}(\epsilon, mix)}{k_{rec}(\epsilon)} \tag{8}$$

This relationship has been analysed in *Wolf et al.* [2019] for the H-mode, following the suggestions in *Fridman and Kennedy* [2004], assuming that the three ratios n_e/N_g, n_e/n_{MI} and k_{eff}/k_{rec} are pressure-independent and $n_e/n_{MI} = 1$ in H-mode. Here we reevaluate this relationship. We have seen in figure 6 that in L-mode and hybrid regime $n_e/n_{MI} \simeq 1$. However, the change of T_g, composition and ϵ in hybrid regime contributes to the increase in k_{eff}. Between 97 and 141 mbar, k_{eff}/k_{rec} increases by one order of magnitude and thus induces the change in ionisation degree from 10^{-5} to 10^{-4} (figure 2). In H-mode, the experimental measurements in figure 2 show that T_g is approximately constant, n_e/N_g is approximately proportional to p and thus n_e is proportional to p^2. Then, the simulation results show that eq. 8 holds with pressure-independent ϵ and mix (approximately constant k_{eff} and k_{rec}) and with n_{MI} (O_2^+) approximately proportional to p, and not p^2 (as pressure increases from 161 to 296 mbar, n_e increases by a factor 3.6 and n_{MI} by a factor 2.4, to reach $n_e/n_{MI} \simeq 1.5$ at 296 mbar), in H-mode, which can only take place because of the emergence of atomic ions. Without this last factor, if n_e/n_{MI} is pressure-independent, k_{eff}/k_{rec} is required to increase further with pressure for the measured dependence $n_e/N_g \propto p$ to be maintained. Although section 4.5 shows that the ion composition, as well as ϵ, and thus k_{eff}, are affected by the uncertainties in the model, our assessment on how the ionisation degree depends on these factors is not altered by the uncertainties.

4.4. Discussion on discharge contraction mechanisms

As in most studies on contraction mechanisms, the CO_2 MW discharge studied in this work contracts under non-uniform gas heating conditions. This is evidenced by the radial profiles of T_g measured in *Wolf et al.* [2020], showing approximately flat distributions of T_g in L-mode conditions and sharp radial gradients in hybrid regime and H-mode conditions. The temperature distributions in the studied conditions are not only the product of MW power absorption, pressure, geometry and finite gas thermal conductivity, but also of the vortex flow and of fast turbulent transport. While the vortex flow contributes to lower the temperature and inject CO_2 near the reactor walls, turbulent transport can contribute to more uniform temperature and composition distributions through fast mixing. The vortex flow is thus an element that contributes to discharge contraction.

The simulation results in figure 4 show that the neutral composition is highly dependent on T_g and on transport, a feature not common in discharge contraction studies so far. As such, in hybrid regime and H-mode conditions, the outer regions of the plasma are significantly less dissociated than the almost-fully-dissociated plasma core. Then, figure 6 shows that the ion composition is highly dependent on T_g, as in *Martinez et al.* [2004]; *Dyatko et al.* [2008]; *Ridenti et al.* [2018] with Ar, and on neutral composition, as proposed in *Martinez et al.* [2009] for different noble gases. Since charged particle kinetics (characteristics times ~ 1 μs) is faster than our estimation of fast transport (~ 100 μs), we expect the ion composition to be molecular in the whole plasma region in L-mode, while at higher pressures more atomic ions are expected in the plasma core than in the outer regions of the plasma, as in *Martinez et al.* [2004]; *Dyatko et al.* [2008]; *Ridenti et al.* [2018]. The ion distribution is particularly important due to the role of molecular ions in charge balance through dissociative recombination. Moreover, figure 9 shows that k_{eff} in the plasma core is significantly higher in H-mode than in L-mode. This is due both to the increase of this coefficient with the degree of dissociation in the plasma as shown in figure 8, and to the increase in T_g. Increasing T_g decreases N_g, which, in agreement with eq. 2, leads to less losses of electron energy and thus allows to reach higher ϵ, as highlighted also by *Martinez et al.* [2004]; *Shneider et al.* [2012]; *Ridenti et al.* [2018]; *Zhong et al.* [2019]. The dependence of k_{eff} on composition as a feature of contraction has also been pointed out in *Zhong et al.* [2019]. The increase of k_{eff} is not expected in the outer regions of the H-mode plasma, where T_g and the dissociation degree are lower.

We conclude that the contraction in hybrid regime and in H-mode is justified by the increases of k_{eff}/k_{rec} (a factor 10 in hybrid regime with standard parameters) and of n_e/n_{MI} (a factor 1.5 in H-mode with standard parameters) in the plasma core with pressure. These are originated by the temperature increase and thus do not take place in the outer regions of the plasma in these regimes. This assessment confirms the claim in *Wolf et al.* [2020] that the appearance of the L- and H-modes results from the evolution of charged particle kinetics in response to the shifting composition. Then, the

contraction is reinforced by power absorption, as MW power is absorbed over a smaller radius in a contracted plasma than in a more diffuse one, as shown in *Kabouzi et al.* [2002]; *Wolf et al.* [2019]. A self-reinforcing cycle is established between heating and ionization, in agreement with *Shneider et al.* [2012, 2014]; *Zhong et al.* [2019].

To evaluate our hypotheses on the factors driving the transition in ionisation degree and contraction mode, we use the model to test the outcome of the simulation with different, possibly unphysical, assumptions. Figure 10 compares the experimentally estimated P_{abs} with simulation results of P_{abs} using different assumptions: i) standard result; ii) fixing composition as pure CO_2 for all 9 cases; iii) fixing composition as 50% CO and 50% O; iv) fixing composition as 1/3 C and 2/3 O; v) fixing T_g at 3322 K, its value at 60 mbar, while fixing composition as 50% CO and 50% O. All input parameters (T_g, n_e, t_r) are the same as in the standard result, except when stated otherwise. Figure 10 allows to assess if each of these assumptions provides values of P_{abs} comparable to the experimental and the standard numerical results or, on the contrary, if unrealistic values of P_{abs} would be necessary to reach the measured electron densities.
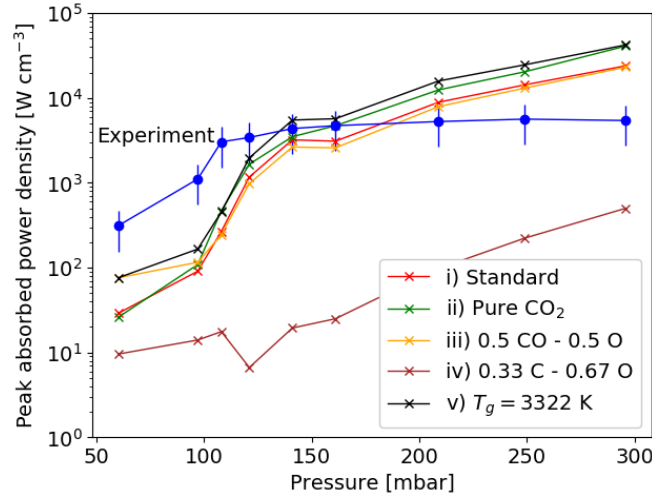

Figure 10. Peak power density P_{abs} from experiments (blue circles) and from simulations (crosses) with assumptions i) to v) explained in the text.

Firstly, figure 10 confirms the importance of gas composition for the ionisation degree. Indeed, if the plasma composition would consist mostly of CO_2, the ion composition would be fully molecular and much higher and more unrealistic values of P_{abs} would be required to reach the ionisation degree measured in H-mode. Hence, dissociation is necessary for mode transition. The result obtained with 1/3 C - 2/3 O composition highlights the influence of mixture, as in that case much lower power densities would be sufficient to obtain the measured n_e. However, small differences in mixture, like the one between the standard case and fixed 50% CO - 50% O, appear to have only a small effect on the output P_{abs}. Moreover, it is interesting to notice the result obtained when fixing T_g to 3322 K while keeping 50% CO - 50% O mixture. Figure 10 shows that even in such a dissociated case, the power densities required

to obtain the measured n_e are much higher with 3322 K than with $\sim$6000 K. These results allow to conclude that non-uniform gas heating and core dissociation are both required to increase k_{eff}, n_e/n_{MI} and thus n_e/N_g in the plasma core, leading to discharge contraction. To our knowledge, it is the first time that dissociation is shown as such an important feature of discharge contraction. Finally, figure 10 shows that the increase in numerical P_{abs} with pressure in H-mode, analysed in section 4.1, holds for different assumptions.

4.5. Effect of uncertainties of input parameters

The model takes gas temperature T_g and electron density n_e as input parameters, as well as the estimation of replacement time t_r. Each of these parameters is subjected to uncertainty. Transport is taken as a loss of all species in the plasma core and the replacement by pure CO_2 in a replacement time t_r, following eq. 1. However, there is a high degree of uncertainty on how convective and diffusive turbulent transport in the microwave vortex flow reactor affects the plasma core. To assess the influence of this uncertainty on the numerical results, we consider, besides the standard values of t_r from table 2, a minimum t_r of 0.1 ms (if lower than standard) and a maximum of 10 ms. Figure 11 shows numerical results using standard input values of T_g and n_e and the three conditions of t_r just described: a) peak power density P_{abs}; b) electron mean energy and E/N_g; c) relative neutral densities; d) densities of main charged species. In each case, the points refer to the cases with standard t_r and the error bars represent the variation between minimum and maximum t_r. Then, Figure 12 assesses the same quantities but considering the error bars in the measurements of T_g, thus taking the standard values of T_g from table 1, a minimum $T_g - \delta_{T_g}$ and a maximum $T_g + \delta_{T_g}$. The results are presented using standard values of t_r and n_e and the three conditions of T_g described previously. Finally, the same is presented in Figure 13 using standard values of t_r and T_g and the standard and limiting conditions of n_e, considering the error bars from the measurements. For the first three pressures (60, 97 and 108 mbar), as δ_{n_e} is higher than standard n_e, the standard value has also been taken as minimum.

Figure 11 shows that the uncertainty associated to transport affects all the results, in the whole pressure range. Indeed, with fast flow, transport is the main mechanism of loss of neutral species (dissociation products) from the plasma core, and their replacement by CO_2. As a result, a short t_r prevents chemical equilibrium and, therefore, leads to a less dissociated plasma, concerning dissociation of CO_2 into CO and O, of O_2 into O and of CO into C and O. At 60 mbar, an almost pure CO_2 plasma is present with $t_r = 0.1$ ms, while a $CO_2/CO/O_2/O$ composition is obtained with $t_r = 10$ ms. At 97 mbar, the CO_2 fraction is variable between 2 and 50%. The uncertainty decreases with pressure and temperature, due to the faster reactivity. In H-mode, for $p \geq 161$ mbar, fractions can vary between 44% and 50% for CO, between 40% and 52% for O and between 0 and 4% for C. The ion composition is directly dependent on the neutral composition. With low t_r, electron-impact ionisation of CO_2, CO and O, together with ion transfers (mainly $CO_2^+ \rightarrow O_2^+$, $CO^+ \rightarrow O^+$ and $O^+ \rightarrow O_2^+$), determine O_2^+ as dominant ion in the whole pressure range. Conversely, with slow transport losses, the dominant ion is mode-dependent, changing from O_2^+ in L-mode to a mixture of O^+ and C^+ in H-mode. In case molecular ions dominate, dissociative recombination has higher reaction rates. Thus, higher E/N_g, ϵ and P_{abs} are necessary for electron-impact ionisation to reach the measured electron densities when faster transport losses are considered. Indeed, at 60 mbar, ϵ can be as high as 2.9 eV with $t_r = 0.1$ ms or as low as 2.1 eV with $t_r = 10$ ms, while at 297 mbar it can vary between 2.7 and 3.1 eV.

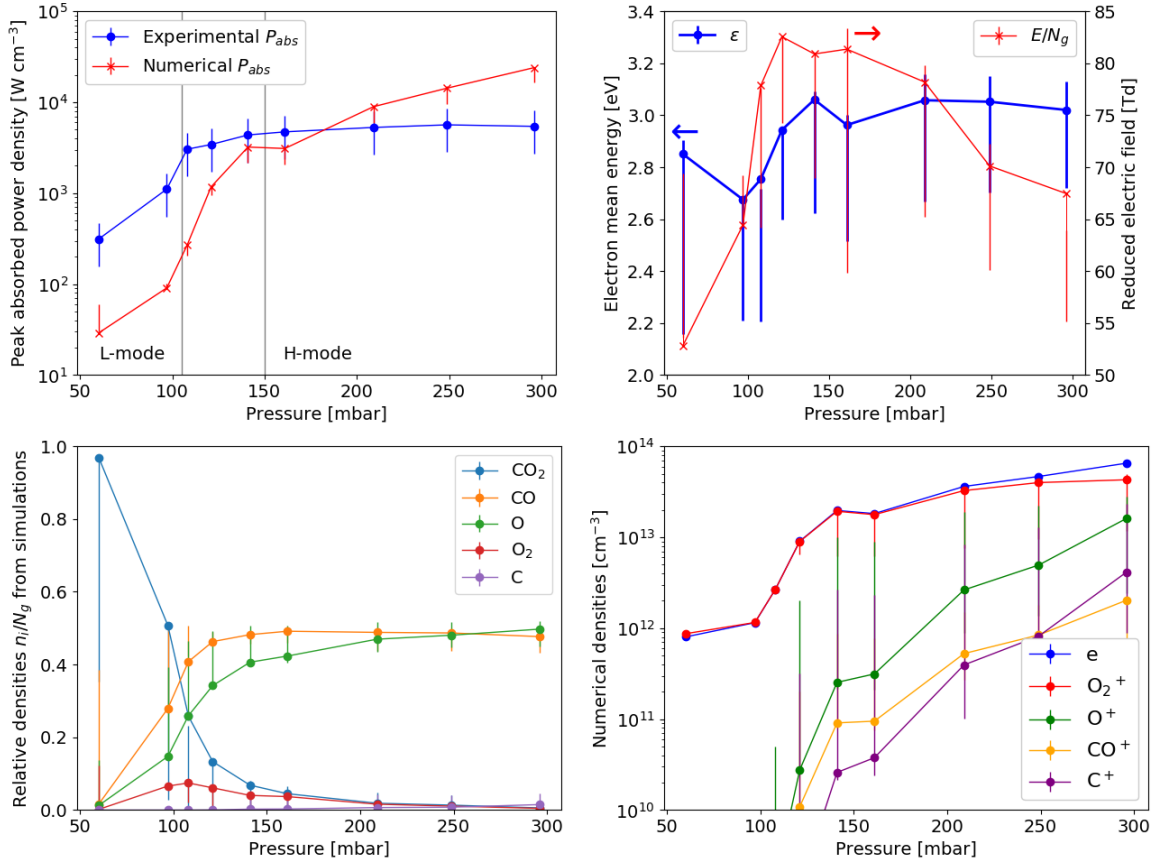**Figure 11.** Simulation results with error bar associated to the uncertainty in t_r used in the model.

Finally, P_{abs} can vary by about one third between the limiting cases of t_r.

Figure 12 shows that, within the limits of the error bars of T_g, with higher T_g, the plasma core is slightly more dissociated, the ion composition in H-mode is more atomic, recombination rates are lower, and so are E/N_g and ϵ. As a result, lower ϵ and P_{abs} are required to reach the measured n_e with $T_g + \delta_{T_g}$. Once again, it is easy to notice the important influence that small changes in T_g and mixture have on the correspondence between ϵ and E/N_g coming from the EEDF solutions. As such, E/N_g, ϵ and P_{abs} end up being the parameters most affected by the uncertainty in T_g, P_{abs} being affected by about one third.

Finally, figure 13 shows that the neutral composition of the plasma core is affected by n_e at 60 mbar, due to electron-impact dissociation. With fast transport losses ($t_r = 0.13$ ms) this effect is very small. However, with one order of magnitude higher t_r, the duplication of n_e (associated with an increase in ϵ) can lead to approximately 20% less CO_2 fraction and 10% more CO fraction in the core. Positive ion densities change with n_e to match quasineutrality, but the ion composition is not affected by the uncertainty. For approximately the same neutral and ion composition, a higher ϵ is required to match a higher n_e. Finally, power density is proportional to both n_e and ϵ and thus can vary significantly between input $n_e - \delta_{n_e}$ and $n_e + \delta_{n_e}$. In fact, for $p \leq 161$
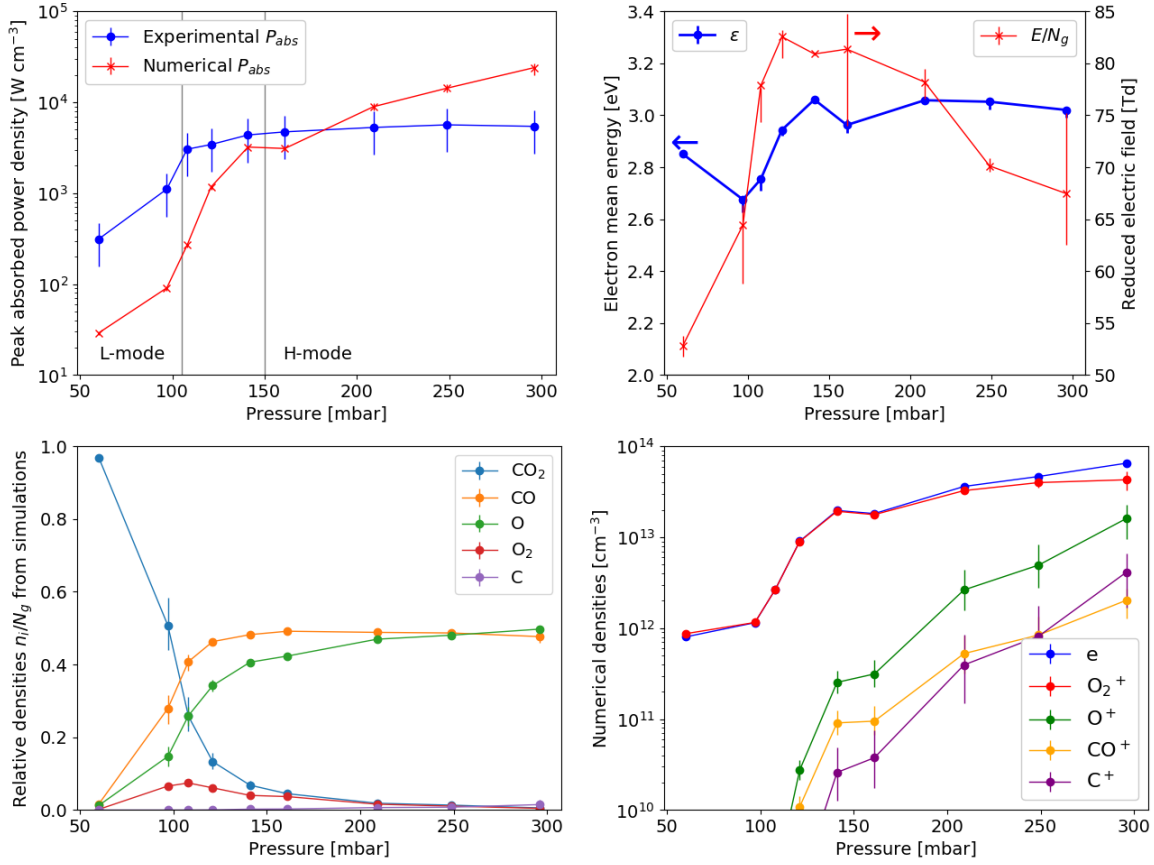
Figure 12. Simulation results with error bar associated to the uncertainty in core gas temperature measured in experiments and used as input in the model.

mbar, the higher limit of the calculated P_{abs} is between 2 and 10 times higher than the lower limit. For higher pressures, the relative difference decreases to about one third at most. The simulation results are thus sensitive to all three input parameters (t_r, T_g and n_e), which reveals the importance of accurately measuring or estimating them, as well as of taking into account their uncertainty when analysing simulation results.
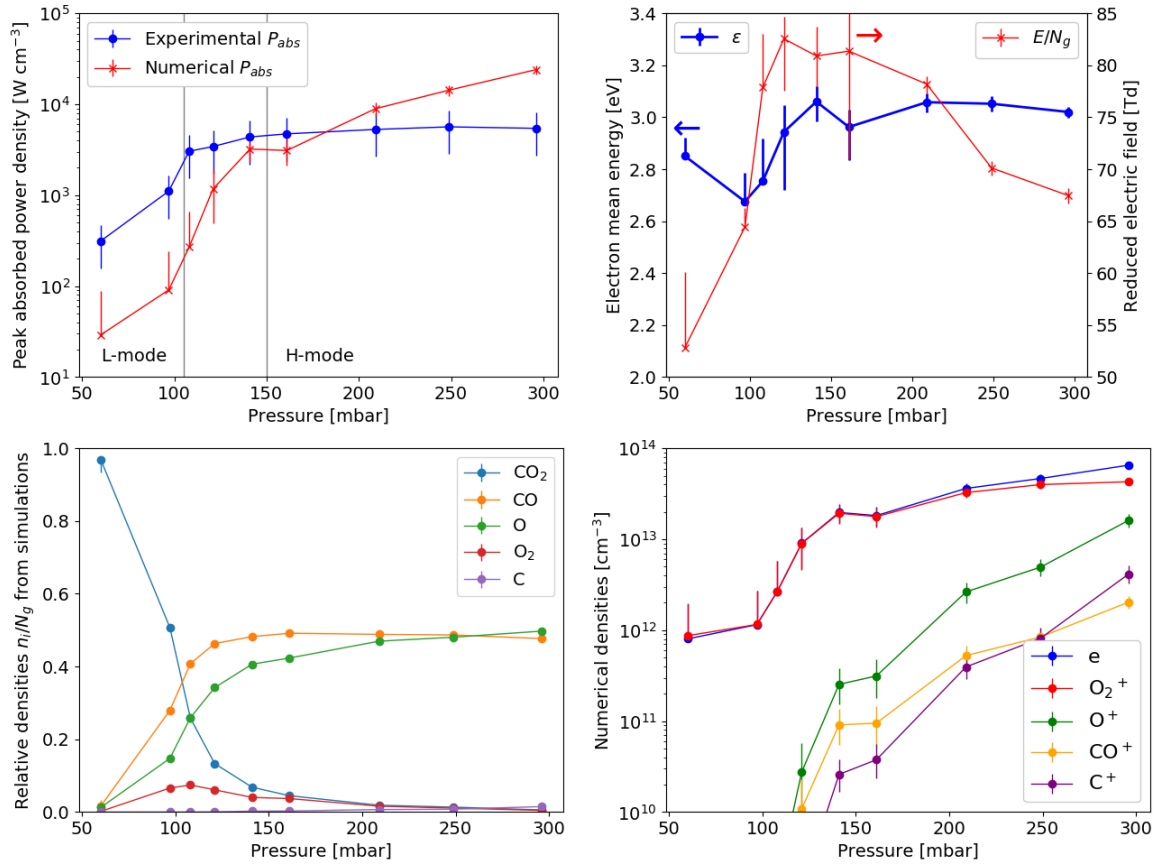
Figure 13. Simulation results with error bar associated to the uncertainty in peak electron density measured in experiments and used as input in the model.

5. Conclusions

This paper addresses plasma chemistry in the core of a microwave discharge for CO_2 conversion. It has focused in particular on the ionisation degree associated to the contraction dynamics of this plasma. In previous works, the homogeneous and contracted L- and H-modes have been observed in experiments, along with a hybrid regime, for a pressure range between 60 and 300 mbar and a temperature range between 3000 and 6500 K. The hybrid regime corresponds to the parameter range where record efficiencies of CO_2 conversion have been registered in several works. Peak gas temperature (T_g), peak electron density (n_e), discharge dimensions and absorbed power density (P_{abs}) have been measured in these conditions in experiments. In this work, a zero-dimensional plasma chemistry model has been developed to simulate the plasma core in the experimentally relevant conditions, taking pressure, T_g and n_e as input parameters, as well as an estimation of replacement time (t_r).

The model describes the kinetics of the main neutral species and charged particles, addressing CO_2 discharges in the temperature range 3000 - 6500 K, with neutral composition ranging from pure CO_2 to mixtures of O/CO/C. The electron kinetics is described through the Monte Carlo Flux method with oscillating electric field. It is the first time that this technique is self-consistently coupled to a complex plasma chemistry model, the EEDF solution being adapted to the wide range of gas mixtures in the addressed conditions. The model has been used for a set of 9 experimental conditions and validated to qualitatively describe the processes taking place in experiments. The validation has been obtained through a comparison between the numerically obtained and the experimentally estimated P_{abs}. Discrepancies between the two quantities have been attributed to limitations in both the numerical and experimental estimations of P_{abs}. Moreover, it has been demonstrated that the uncertainties in the input parameters of the model T_g, n_e and t_r have a significant effect on the model results. Thus, it is important to increase accuracy on these parameters and to take uncertainties into account when assessing numerical results and comparing them with experiments.

The simulation results have shown that the transition from L- to H-mode is accompanied by a transition in neutral composition. While the homogeneous and L-modes are characterised by a significant amount of CO_2 and O_2, the H-mode corresponds to a completely dissociated plasma core, composed mostly of CO and O, possibly with a relevant amount of C. The neutral composition in the core is determined mostly by neutral thermal chemistry and by transport processes. Electron-impact dissociation of CO_2, O_2 and CO contributes to a more dissociated composition. However, its role is secondary and only causes a moderate change in composition at low pressure, where T_g is low ($\simeq 3000$ K) and neutral chemistry is slow (ms timescale). The ion composition in the core has been shown to be dependent on neutral composition and, thus, to tendentiously change from molecular (dominant ion O_2^+) to atomic (O^+ and C^+) with mode transition. This result has been attributed to electron-impact ionisation, ion transfer and dissociative recombination reactions. These reactions are directly related

with the transition in ionisation degree in the core from 10^{-5} to 10^{-4} that sustains the contracted mode transition. Indeed, the simulations have shown that the increase in T_{g} from L- to H-mode drives dissociation and decreases electron energy losses. These factors are fundamental to an increase in the effective electron-impact ionisation coefficient. Moreover, the relative importance of electron losses through recombination of molecular ions is lower in H-mode than in L-mode, due to the change in ion composition.

As a result of the combined experimental and numerical study, we have developed our understanding of the CO_2 microwave discharge contracted mode transitions. It is based on and expands upon the existing theories of discharge contraction in simpler systems and it is summarised as follows. The increase of pressure leads to higher electron-driven collisionality and then to a change in gas temperature in the plasma core from around the threshold of CO_2 dissociation (~ 3000 K) to around the threshold of CO dissociation (~ 6000 K), with corresponding change in mixture. Radial heat losses in the vortex flow configuration impose sharp temperature gradients at high pressure. The buildup of temperature in the core and corresponding decrease of gas density allows to lower the losses of electron energy. The change in electron energy and composition favours higher electron-impact ionisation rates and relatively lower recombination between electrons and molecular ions in the core. These factors lead to an increase of the peak ionisation degree from 10^{-5} to 10^{-4} in the pressure range from 97 to 121 mbar and to keeping it approximately proportional to pressure in H-mode. These conditions do not take place in the outer regions of the plasma where temperature is lower, giving rise to the contracted plasma shape. This is linked to the absorption of higher P_{abs} in the core and thus to the reduction of the skin-depth of wave absorption, that generates a self-reinforcing cycle of electron-driven collisionality and gas heating. One hypothesis to dimensionally upscale plasma-driven conversion of CO_2 stems from this study. Keeping conditions of high thermal dissociation in the plasma core and decreasing microwave frequency, may lead to increasing the discharge radius and obtaining higher CO output.

Acknowledgments

References

Albritton, D. L. (1978), Ion-neutral reaction-rate constants measured in flow reactors through 1977, *At. Data Nucl. Data Tables*, *22*, 1–101.

Alves, L., P. Coche, M. A. Ridenti, and V. Guerra (2016), Electron scattering cross sections for the modelling of oxygen-containing plasmas, *Eur. Phys. J. D*, *70*(124), www.lxcat.net/IST-Lisbon, retrieved on January 30, 2020.

Alves, L. L. (2014), The IST-Lisbon database on LXCat, *J. Phys. Conf. Series*, *565*(1), www.lxcat.net/IST-Lisbon, retrieved on January 30, 2020.

Asisov, R. I., A. A. Fridman, V. K. Givotov, E. G. Krsheninnikov, B. I. Patrushev, B. V. Potapkin, V. D. Rusanov, and M. F. Krotov (1981), Carbon dioxide dissociation in nonequilibrium plasma, *5th International Symposium on Plasma Chemistry*, *2*, 774–779.

Baulch, D. L., D. D. Drysdale, J. Duxbury, and S. J. Grant (1976), *Evaluated kinetic data for high temperature reactions, vol. 3: Homogeneous gas phase reactions of O_2-O_3 system, CO-O_2-H_2 system, and of sulphur-containing species*, Buttersworth, Toronto.

Berthelot, A., and A. Bogaerts (2016), Modeling of plasma-based CO_2 conversion: lumping of the vibrational levels, *Plasma Sources Sci. Technol.*, *25*(045022).

Berthelot, A., and A. Bogaerts (2018), Pinpointing energy losses in CO_2 plasmas - Effect on CO_2 conversion, *Journal of CO_2 Utilization*, *24*, 479–499.

Beuthe, T. G., and J. S. Chang (1997), Chemical kinetics modelling of non-equilibrium Ar-CO_2 thermal plasmas, *Jpn. J. Appl. Phys.*, *36*, 4997–5002.

Biagi (2019), Biagi database (trascription of data from S. F. Biagi's Fortran code Magboltz), www.lxcat.net/Biagi, retrieved on December 18, 2019.

Bílek, P., M. Simek, and Z. Bonaventura (2019), Electric field determination from intensity ratio of n_2^+ and n_2 bands: nonequilibrium transient discharges in pure nitrogen, *Plasma Sources Sci. Technol.*, *28*(115011).

Bongers, W., H. Bouwmeester, B. Wolf, F. Peeters, S. Welzel, D. C. M. van den Bekerom, N. den Harder, A. Goede, M. Graswinckel, P. W. Groen, J. Kopecki, M. Leins, G. van Rooij, A. Schulz, M. Walker, and R. van de Sanden (2017), Plasma-driven dissociation of CO_2 for fuel synthesis, *Plasma Process. Polym.*, *14*(e1600126).

Braglia, G. L., and L. Romanò (1984), Monte Carlo and Boltzmann two-term calculations of electron transport in CO_2, *Lettere Al Nuovo Cimento*, *40*, 513–518.

Butylkin, Y. P., A. A. Grinenko, A. A. Levitskii, L. S. Polak, N. M. Rytova, and D. I. Slovetskii (1979), Mathematical modeling of the kinetics of the thermal decomposition of carbon dioxide in an electric arc discharge and quenching of the products, *Khimiya Vysokikh Énergii*, *13*, 545–551.

Butylkin, Y. P., V. K. Zhivotov, E. G. Krasheninnikov, M. F. Krotov, V. D. Rusanov, Y. V. Tarasov, and A. A. Fridman (1981), Dissociation of CO_2 by a plasma-chemical process in a nonequilibrium microwave discharge, *Sov. Phys. Tech. Phys.*, *26*, 555–558.

Capitelli, M., R. Celiberto, G. Colonna, F. Esposito, C. Gorse, K. Hassouni, A. Laricchiuta, and S. Longo (2015), *Fundamental aspects of plasma chemical physics: kinetics*, vol. 85, Springer Science & Business Media.

Cenian, A., A. Chernukho, V. Borodin, and G. Sliwinski (1994), Modeling of plasma-chemical reactions in gas mixture of CO_2 laser I. Gas decomposition in pure CO_2 glow discharge, *Contrib. Plasma Phys.*, *34*, 25–37.

Chang, F., and V. K. Dhir (1995), Mechanisms of heat transfer enhancement and slow decay of swirl in tubes using tangential injection, *International Journal of Heat and Fluid Flow*, *16*, 78–87.

den Harder, N., D. C. M. van den Bekerom, R. S. Al, M. F. Graswinckel, J. M. Palomares, F. J. J. Peeters, S. Ponduri, T. Minea, W. A. Bongers, M. C. M. van de Sanden, and G. J. van Rooij (2017), Homogeneous CO_2 conversion by microwave plasma: Wave propagation and diagnostics, *Plasma Process. Polym.*, *14* (e1600120).

Dyatko, N. A., Y. Z. Ionikh, I. V. Kochetov, D. L. Marinov, A. V. Meshchanov, A. P. Napartovich, F. B. Petrov, and S. A. Starostin (2008), Experimental and theoretical study of the transition between diffuse and contracted forms of the glow discharge in argon, *J. Phys. D: Appl. Phys.*, *41* (055204).

Fairbairn, A. R. (1969), The dissociation of carbon monoxide, *Proc. Roy. Soc. A*, *312*, 207–227.

Fleisch, T., Y. Kabouzi, M. Moisan, J. Pollak, E. C. Martinez, H. Nowakowska, and Z. Zakrzewski (2007), Designing an efficient microwave-plasma source, independent of operating conditions, at atmospheric pressure, *Plasma Sources Sci. Technol.*, *16*, 173–182.

Fontijn, A., A. Fernandez, A. Ristanovic, M. Y. Randall, and J. T. Jankowiak (2001), CO chemiluminescence and kinetics of the $C_2 + O_2$ reaction, *J. Phys. Chem. A*, *105*, 3182–3189.

Fridman, A. (2008), *Plasma chemistry*, Cambridge University Press.

Fridman, A., and L. A. Kennedy (2004), *Plasma physics and engineering*, Taylor and Francis Routledge.

Goede, A., and M. C. M. van de Sanden (2016), CO_2-neutral fuels, *Europhys. News*, *47*, 22–26.

Goede, A. P. H., W. A. Bongers, M. F. Graswinckel, M. C. M. van de Sanden, M. Leins, J. Kopecki, A. Schulz, and M. Walker (2014), Production of solar fuels by CO_2 plasmolysis, *EPJ Web of Conferences*, *79* (01005).

Golubovskii, Y. B., V. Nekuchaev, S. Gorchakov, and D. Uhrlandt (2011), Contraction of the positive column of discharges in noble gases, *Plasma Sources Sci. Technol.*, *20* (053002).

Golubovskii, Y. B., A. V. Siasko, and V. Nekuchaev (2019), Role of thermal effects in neon and argon constricted discharges, *Plasma Sources Sci. Technol.*, *28* (045007).

Golubovskii, Y. B., A. V. Siasko, and V. Nekuchaev (2020), Peculiarities of glow discharge constriction in helium, *Accepted on Plasma Sources Sci. Technol.*

Gordon, S., and B. J. McBride (1994), Computer program for calculation of complex chemical equilibrium compositions and applications, https://cearun.grc.nasa.gov/.

Groen, P. W. C., A. J. Wolf, T. W. H. Righart, M. C. M. van de Sanden, F. J. J. Peeters, and W. A. Bongers (2019), Numerical model for the determination of the reduced electric field in a CO_2 microwave plasma derived by the principle of impedance matching, *Plasma Sources Sci. Technol.*, *28*(075016).

Gudmundsson, J. T., and E. G. Thorsteinsson (2007), Oxygen discharges diluted with argon: dissociation processes, *Plasma Sources Sci. Technol.*, *16*, 399–412.

Guerra, V., T. Silva, P. Ogloblina, M. Grofulovć, L. Terraz, M. L. da Silva, C. D. Pintassilgo, L. L. Alves, and O. Guaitella (2017), The case for in situ resource utilisation for oxygen production on Mars by non-equilibrium plasmas, *Plasma Sources Sci. Technol.*, *26*, 11LT01.

Guerra, V., A. T. del Caz, C. D. Pintassilgo, and L. L. Alves (2019), Modelling N_2-O_2 plasmas: volume and surface kinetics, *Plasma Sources Sci. Technol.*, *28*(073001).

Hagelaar, G., and L. Pitchford (2005), Solving the Boltzmann equation to obtain electron transport coefficients and rate coefficients for fluid models, *Plasma Sources Sci. Technol.*, *14*(722).

Hairer, E. (2004), Radau5 solver, www.unige.ch/~hairer/software.html.

Hairer, E., and G. Wanner (1996), *Solving ordinary differential equations II: Stiff and differential algebraic problems*, Springer-Verlag.

Hippler, H., R. Rahn, and J. Troe (1990), Temperature and pressure dependence of ozone formation rates in the range 1-1000 bar and 90-370 K, *J. Chem. Phys.*, *93*, 6560–6569.

Hokazono, H., and H. Fujimoto (1987), Theoretical analysis of the CO_2 molecule decomposition and contaminants yield in transversely excited atmospheric CO_2 laser discharge, *J. Appl. Phys.*, *62*, 1585–1594.

Husain, D., and L. J. Kirsch (1971), Reactions of tomic carbon $C(2^3p_j)$ by kinetic absorption spectroscopy in the vacuum ultra-violet, *Trans. Farad Soc.*, *67*, 2025–2035.

Itikawa, Y. (2015), Cross sections for electron collisions with carbon monoxide, *J. Phys. Chem. Ref. Data*, *44*(013105), www.lxcat.net/Itikawa, retrieved on December 18, 2019.

Kabouzi, Y., M. D. Calzada, M. Moisan, K. C. Tran, and C. Trassy (2002), Radial contraction of microwave-sustained plasma columns at atmospheric pressure, *J. Appl. Phys.*, *91*, 1008–1019.

Kee, R. J., F. M. Rupley, J. A. Miller, M. E. Coltrin, J. F. Grcar, E. Meeks, H. K. Moffat, A. E. Lutz, G. Dixon-Lewis, M. D. Smooke, J. Warnatz, G. H. Evans, R. S. Larson, R. E. Mitchell, L. R. Petzold, W. C. Reynolds,

M. Caracotsios, W. E. Stewart, P. Glarborg, C. Wang, and O. Adigun (2000), Chemkin collection, Release 3.6, Reaction Design, Inc., San Diego, CA, https://www3.nd.edu/ powers/ame.60636/chemkin2000.pdf.

Kenty, C. (1962), Volume recombination, constriction and volt-ampere characteristics of the positive column, *The Physical Review*, *126*, 1235–1238.

Koelman, P., S. Heijkers, S. T. Mousavi, W. Graef, D. Mihailova, T. Kozák, A. Bogaerts, and J. van Dijk (2017), A comprehensive model for the splitting of CO_2 in non-equilibrium plasmas, *Plasma Process. Polym.*, *14*(1600155).

Kossyi, A., A. Y. Kostinsky, A. A. Matveyev, and V. P. Silakov (1992), Kinetic scheme of the non-equilibrium discharge in nitrogen-oxygen mixtures, *Plasma Sources Sci. Technol.*, *1*, 207–220.

Kotov, V., and P. M. J. Koelman (2019), Plug flow reactor model of the plasma chemical conversion of CO_2, *Plasma Sources Sci. Technol.*, *28*(095002).

Kozák, T., and A. Bogaerts (2014), Splitting of CO_2 by vibrational excitation in non-equilibrium plasmas: a reaction kinetics model, *Plasma Sources Sci. Technol.*, *23*(045004).

Kwak, H. S., H. S. Uhm, Y. C. Hong, and E. H. Choi (2015), Desintegration of carbon dioxide molecules in a microwave plasma torch, *Nature Scientific Reports*, *5*(18436).

Legasov, V. A., V. K. Zhivotov, E. G. Krasheninnikov, M. F. Krotov, B. I. Patrushev, V. D. Rusanov, G. V. Rykunov, A. M. Spektor, A. A. Fridman, and G. V. Sholin (1978), A nonequilibrium plasma-chemical process of CO_2 dissociation in high-frequency and ultra-high-frequency discharges, *Dokl. Akad. Nauk*, *238*, 66–69.

Lindemann, F. (1922), Discussion on "The radiation theory of chemical action", *Trans. Farad Soc.*, *17*, 598–606.

Longo, S. (2006), Monte Carlo simulation of charged species kinetics in weakly ionized gases, *Plasma Sources Sci. Technol.*, *15*, S181–S188.

MAGBOLTZ (2019), Fortran program, MAGBOLTZ version 8.9, S. F. Biagi, http://magboltz.web.cern.ch/magboltz/ (last access 18/12/2019).

Martinez, E. C., Y. Kabouzi, K. Makasheva, and M. Moisan (2004), Modeling of microwave-sustained plasmas at atmospheric pressure with application to discharge contraction, *Phys. Rev. E*, *70*(066405).

Martinez, E. C., M. Moisan, and Y. Kabouzi (2009), Achieving non-contracted and non-filamentary rare-gas tubular discharges at atmospheric pressure, *J. Phys. D: Appl. Phys.*, *42*(012003).

Mcelroy, D., C. Walsh, A. J. Markwick, M. A. Cordiner, K. Smith, and T. J. Millar (2013), The UMIST database for astrochemistry 2012, *Astron. Astrophys.*, *550*(A36).

Mitchell, J. B. A., and H. Hus (1985), The dissociative recombination and excitation of CO^+, *J. Phys. B: At. Mol. Phys.*, *18*, 547–555.

Moisan, M., and J. Pelletier (2012), *Physics of collisional plasmas: Introduction to high-frequency discharges*, 369-385 pp., Springer.

Nantel-Valiquette, M., Y. Kabouzi, E. Castaños-Martinez, K. Makasheva, M. Moisan, and J. C. Rostaing (2006), Reduction of perfluorinated compound emissions using atmospheric pressure microwave plasmas: Mechanisms and energy efficiency, *Pure Appl. Chem.*, *78*, 1173–1185.

Obrusník, A., P. Bílek, T. Hoder, M. Simek, and Z. Bonaventura (2018), Electric field determination in air plasmas from intensity ratio of nitrogen spectral bands: I. sensitivity analysis and uncertainty quantification of dominant processes, *Plasma Sources Sci. Technol.*, *27*(085013).

Ogloblina, P., A. T. del Caz, V. Guerra, and L. L. Alves (2020), Electron impact cross sections for carbon monoxide and their importance in the electron kinetics of CO_2-CO mixtures, *Plasma Sources Sci. Technol.*, *29*(015002).

Pancheshnyi, S., S. Biagi, M. Bordage, G. Hagelaar, W. Morgan, A. Phelps, and L. Pitchford (2012), The LXCat project: Electron scattering cross sections and swarm parameters for low temperature plasma modeling, *Chemical Physics*, *398*, 148.

Park, C., J. T. Howe, and R. L. Jaffe (1994), Review of chemical-kinetic problems of future NASA missions, II: Mars entries, *J. Thermophys. Heat Tr.*, *8*, 9-23.

Petrov, G. M., and C. M. Ferreira (1999), Numerical modeling of the constriction of the dc positive column in rare gases, *Phys. Rev. E*, *59*, 3571–3582.

Pietanza, L. D., G. Colonna, and M. Capitelli (2020), Kinetics versus thermodynamics on CO_2 dissociation in high temperature microwave discharges, *Plasma Sources Sci. Technol.*, *29*(035022).

Ridenti, M. A., J. D. Amorim, A. D. Pino, V. Guerra, and G. Petrov (2018), Causes of plasma column contraction in surface-wave-driven discharges in argon at atmospheric pressure, *Phys. Rev. E*, *97*(013201).

Schaefer, G., and P. Hui (1990), The Monte Carlo flux method, *J. Comput. Phys.*, *89*, 1–30.

Shneider, M. N., M. S. Mokrov, and G. M. Milikh (2012), Dynamic contraction of the positive column of a self-sustained glow discharge in molecular gas, *Phys. Plasmas*, *19*(033512).

Shneider, M. N., M. S. Mokrov, and G. M. Milikh (2014), Dynamic contraction of the positive column of a self-sustained glow discharge in air flow, *Phys. Plasmas*, *21*(032122).

Slack, M. W. (1976), Kinetics and thermodynamics of the CN molecule. III. Shock tube measurements of CN dissociation rates, *J. Chem. Phys.*, *64*, 228–236.

Smith, G. P., D. M. Golden, M. Frenklach, N. W. Moriarty, B. Eiteneer, M. Goldenberg, C. T. Bowman, R. K. Hanson, S. Song, W. C. G. Jr., V. V. Lissianski, and Z. Qin (2018), Gri-mech 3.0, http://combustion.berkeley.edu/gri-mech/version30/text30.html.

Snoeckx, R., and A. Bogaerts (2017), Plasma technology - a novel solution for CO_2 conversion?, *Chem. Soc. Rev.*, *46*, 5805–5863.

Sun, H., J. Lee, H. Do, S.-K. Im, and M. S. Bak (2017), Experimental and numerical studies on carbon dioxide decomposition in atmospheric electrodeless microwave plasmas, *J. Appl. Phys.*, *122*(033303).

Tejero-del Caz, A., V. Guerra, D. Gonçalves, M. L. da Silva, L. Marques, N. Pinhão, C. D. Pintassilgo, and L. L. Alves (2019), The LisbOn KInetics Boltzmann solver, *Plasma Sources Sci. Technol.*, *28*(043001), https://github.com/IST-Lisbon/LoKI (last access 29/08/2019).

Trenchev, G., S. Kolev, W. Wang, M. Ramakers, and A. Bogaerts (2017), CO_2 conversion in a gliding arc plasmatron: multidimensional modeling for improved efficiency, *J. Phys. Chem. C*, *121*, 24470–24479.

van den Bekerom, D. C. M., J. M. P. Linares, T. Verreycken, E. M. van Veldhuizen, S. Nijdam, G. Berden, W. A. Bongers, M. C. M. van de Sanden, and G. J. van Rooij (2019), The importance of thermal dissociation in CO_2 microwave discharges investigated by power pulsing and rotational Raman scattering, *Plasma Sources Sci. Technol.*, *28*(055015).

van den Bekerom, D. C. M., A. van de Steeg, M. C. M. van de Sanden, and G. J. van Rooij (2020), Mode resolved heating dynamics in pulsed microwave CO_2 plasma from laser Raman scattering, *J. Phys. D: Appl. Phys.*, *53*(054002).

van Rooij, G. J., D. C. M. van den Bekerom, N. den Harder, T. Minea, G. Berden, W. A. Bongers, R. Engeln, M. F. Graswinckel, E. Zoethout, and M. C. M. van de Sanden (2015), Taming microwave plasma to beat thermodynamics in CO_2 dissociation, *Faraday Discuss.*, *183*, 233–248.

Vialetto, L., S. Longo, and P. Diomede (), *in preparation*.

Vialetto, L., S. Longo, and P. Diomede (2019), Benchmark calculations for electron velocity distribution function obtained with Monte Carlo Flux simulations, *Plasma Sources Sci. Technol.*, *28*(115015).

Viegas, P., M. C. M. van de Sanden, S. Longo, and P. Diomede (2019), Validation of the Fokker–Planck approach to vibrational kinetics in CO_2 plasma, *J. Phys. Chem. C*, *123*, 22823–22831.

Wang, W., and A. Bogaerts (2016), Effective ionisation coefficients and critical breakdown electric field of CO_2 at elevated temperature: effect of excited states and ion kinetics, *Plasma Sources Sci. Technol.*, *25*(055025).

Wang, W., A. Berthelot, S. Kolev, X. Tu, and A. Bogaerts (2016), CO_2 conversion in a gliding arc plasma: 1D cylindrical discharge model, *Plasma Sources Sci. Technol.*, *25*(065012).

Wolf, A. J., T. W. H. Righart, F. J. J. Peeters, P. W. C. Groen, M. C. M. van de Sanden, and W. A. Bongers (2019), Characterization of CO_2 microwave plasma based on the phenomenon of skin-depth-limited contraction, *Plasma Sources Sci. Technol.*, *28*(115022).

Wolf, A. J., T. W. H. Righart, F. J. J. Peeters, W. A. Bongers, and M. C. M. van de Sanden (2020), Implications of thermo-chemical instability on the contracted modes in CO_2 microwave plasmas, *Plasma Sources Sci. Technol.*, *29*(025005).

Zatsarinny, O., and K. Bartschat (2004), B-spline Breit–Pauli R-matrix calculations for electron collisions with argon atoms, *J. Phys. B: At. Mol. Opt. Phys.*, *37*(4693), www.lxcat.net/BSR, retrieved on December 18, 2019.

Zhong, H., M. N. Shneider, M. S. Mokrov, and Y. Ju (2019), Thermal-chemical instability of weakly ionized plasma in a reactive flow, *J. Phys. D: Appl. Phys.*, *52*(484001).